

A chemical approach to 2D-2D heterostructures beyond van der Waals: high-throughput on-device covalent connection of MoS₂ and graphene

Manuel Vázquez Sulleiro¹, Aysegul Develioglul¹, Ramiro Quirós-Ovies^{1,4}, Natalia Martín Sabanés¹, I. Jéniffer Gómez², Mariano Vera-Hidalgo¹, Víctor Sebastián^{3,4}, Jesús Santamaría^{3,4,5}, Enrique Burzuri^{1*}, and Emilio M. Pérez^{1,*}

E-mail: enrique.burzuri@imdea.org, emilio.perez@imdea.org

¹IMDEA Nanociencia C/Faraday 9 Ciudad Universitaria de Cantoblanco, 28049 Madrid, Spain.

²CEITEC Masaryk University Kamenice 5, 62500 Brno, Czech Republic.

³Department of Chemical and Environmental Engineering Universidad de Zaragoza Campus Rio Ebro, 50018 Zaragoza, Spain.

⁴Instituto de Nanociencia y Materiales de Aragon (INMA), CSIC-Universidad de Zaragoza, 50009 Zaragoza, Spain.

⁵Networking Research Center on Bioengineering, Biomaterials and Nanomedicine (CIBER-BBN), 28029 Madrid, Spain.

ABSTRACT:

The most widespread method for the synthesis of 2D-2D heterostructures is the direct growth of one material on top of the other. Alternatively, one can manually stack flakes of different materials. Both methods are limited to one crystal/device at a time and involve interfacing the 2D materials through van der Waals forces, to the point that all these materials are known as van der Waals heterostructures. Synthetic chemistry is the paradigm of atomic-scale control, yet its toolbox remains unexplored for the construction of 2D-2D heterostructures. Here, we describe how to covalently connect 2H-MoS₂ flakes to several single-layer graphene field-effect transistors simultaneously, and show that the final electronic properties of the MoS₂-graphene heterostructure are dominated by the molecular interface.

We use a bifunctional molecule with two chemically orthogonal anchor points, selective for sulphides and carbon-based materials. Our experiments highlight the potential of the chemical approach to build 2D-2D heterostructures beyond van der Waals.

INTRODUCTION:

The combination of nanomaterials is a promising approach towards materials made by design. In particular, the stack of different 2D materials has attracted enough attention to inaugurate a field of research: van der Waals heterostructures¹. These are typically synthesised either by van der Waals epitaxy², or by deterministic placement of flake(s) of one material on top of the other^{1,3,4,5,6,7}. Within 2D-2D van der Waals heterostructures, the combination of transition metal dichalcogenides (TMDCs) and graphene is a particularly active area of research, as the combination of the semiconducting properties of TMDCs with the high carrier mobility of graphene is particularly attractive for applications^{8,9,10,11,12}. Several TMDC-TMDC heterojunctions have also been described^{13,14,15}. Although this strategy has proven promising for the construction of high-performance devices, in all cases the 2D layers are relatively weakly bonded and can be taken apart in some solvents or thermal processes^{16,17}, plus it suffers from a complete lack of control over the interface between nanomaterials in terms of electronic communication, chemical nature, and interlayer distance.

In order to overcome these shortcomings, we decided to explore covalent chemistry as an alternative method for the connection of 2D materials, using a molecule with two anchor points. On one hand, we exploit the chemistry of maleimide described by our group to functionalize sulphide-based materials under mild conditions^{18,19,20,21}. On the other hand, we use a diazonium salt^{22,23,24}, which is the most common method for the covalent modification graphene^{25,26}. The solvents play a key role to activate a specific part of the molecule for the covalent anchoring.

RESULTS AND DISCUSSION

Functionalization and characterization of MoS₂

Liquid phase exfoliation (LPE) of bulk MoS₂ was performed using an ultrasonic probe (1h) in N-Methyl-2-pyrrolidone (NMP). Unexfoliated material was separated through centrifugation, yielding a black supernatant which was stable in the NMP suspension. This suspension was filtered, and the resulting exfoliated pristine material (*p*-MoS₂) presented a 2H polymorphism, as confirmed by Raman spectroscopy with the characteristic modes of 2H-MoS₂, UV-Vis extinction showing the characteristic excitonic transitions, and XRD patterns in good agreement with the standard data for MoS₂ (Supplementary Fig. 1-4)²⁷. Besides, *p*-MoS₂ showed a Raman shift of 4 cm⁻¹ in the in-plane E_{12g} and out-of-plane A_{1g}, compared to bulk MoS₂ due to the exfoliation process. To functionalize *p*-MoS₂, the suspended material was transferred to a dry CH₃CN solution of phenylmaleimide diazonium (**1**) and the mixture was vigorously stirred overnight in the absence of light, to prevent activation of the diazonium group (Figure 1a)²⁸. The mixture was filtered, and the solid washed several times with CH₃CN to remove unreacted **1**. The effectiveness of the washing progress was verified by UV-Vis (Supplementary Fig. 5), confirming the absence of maleimide after three washes. Considering the rich reactivity of diazonium compounds^{28,29,30}, we also made sure that the diazonium group **1** remained stable under the maleimide-MoS₂ reaction conditions: 90% of the reagent was recovered from the washing solutions after the reaction, Nuclear magnetic resonance (NMR) spectroscopy and Fourier Transform Infrared Spectroscopy (FTIR) confirmed the presence of the diazonium group (Supplementary Fig. 6-7).

FTIR of the MoS₂ sample functionalized (*f*-MoS₂) with **1** shows conclusive evidence of C-S bond formation (Figure 1b). The presence of the carbonyl stretch of the maleimide (1714 cm⁻¹) is only observed in the modified MoS₂ (1712 cm⁻¹). Moreover, the C-H bending mode of the alkene (black trace, 841 cm⁻¹) disappears after the reaction with MoS₂. Functionalized material showed a new band assigned to the new C-S bond generated (724 cm⁻¹), confirming the connection between the organic moiety and the material¹⁹. A control experiment where *p*-MoS₂ was subjected to the same reaction protocol in the absence of **1** did not show any of these spectroscopic features. Thermogravimetric

analysis (Supplementary Fig. 8) showed clear differences between the functionalized and pristine material, mainly with a first weight loss from 240 °C to 340 °C, which can be attributed to the decomposition of the organic molecule anchored to the MoS₂ (Supplementary Fig. 8, orange trace). The following reaction process, between 360 to 560 °C, occurs due to the oxidation of MoS₂; a final pronounced drop from 630 °C to 780 °C is observed, where the total burning of the sample occurs. In addition, at 600 °C the weight loss difference between pristine material against *f*-MoS₂ is 5%. To further investigate the elemental composition and its chemical state, X-ray photoelectron spectroscopy (XPS) was performed. The elemental analysis survey (Table S1) showed in the case of *f*-MoS₂ the presence of N (1.3 %, N 1s, 400.6 eV), B (0.6%, B 1s, 194.6 eV) and F (2.4%, F 1s, 686.8) with atomic ratios in good keeping with the chemical composition of the functionalizing moiety, suggesting the anchoring of the molecule to the surface of the material, including the unreacted diazo group (Supplementary Fig. 9). Fitting the S 2p core level spectra we can observe the characteristic doublet feature in the *p*-MoS₂, in the case of *f*-MoS₂ the peak becomes broader and requires a new component usually assigned to the S-C new bond generated in the covalent functionalization of the MoS₂ (Supplementary Fig. 10)^{19,31,32}.

Raman spectroscopy measurements ($\lambda_{\text{exc}} = 633 \text{ nm}$) revealed the stability of the 2H-polytype after the functionalization (Figure 1c and Supplementary Fig. 11 for further details). The main in-plane E_{2g}^1 and out-of-plane A_{1g} Raman modes are clearly observed. Additional complex second order double resonant peaks at around 170, 460 and 600 cm⁻¹ appear due to the resonant excitation condition^{33,34,35}, and decrease in intensity with respect to the A_{1g} mode upon functionalization. Suppression of the second order resonant modes in the functionalized MoS₂ can be attributed to alteration of the resonant conditions upon functionalization, and is consistent with the shift of the peak around 633 nm in the UV-Vis absorption spectra (see Supplementary Fig. 12 for details). Similarly, the decrease of the complex mode at 460 cm⁻¹ (2LA(M)) has been used as a marker of functionalization of MoS₂ elsewhere³⁴. Additional changes between the Raman spectra of pristine

and functionalised MoS₂ are discussed in detail in the Supplementary information. Surface-enhanced Raman spectroscopy (SERS) analysis provides further indication of functionalization. In particular, SERS spectra of maleimide molecules in comparison with pristine and functionalized MoS₂, reveal enhanced Raman bands in the *f*-MoS₂ sample (notably at 1372 and 1601 cm⁻¹) attributed to the succinimide molecules, which is absent in the case of *p*-MoS₂ (Supplementary Fig. 13).

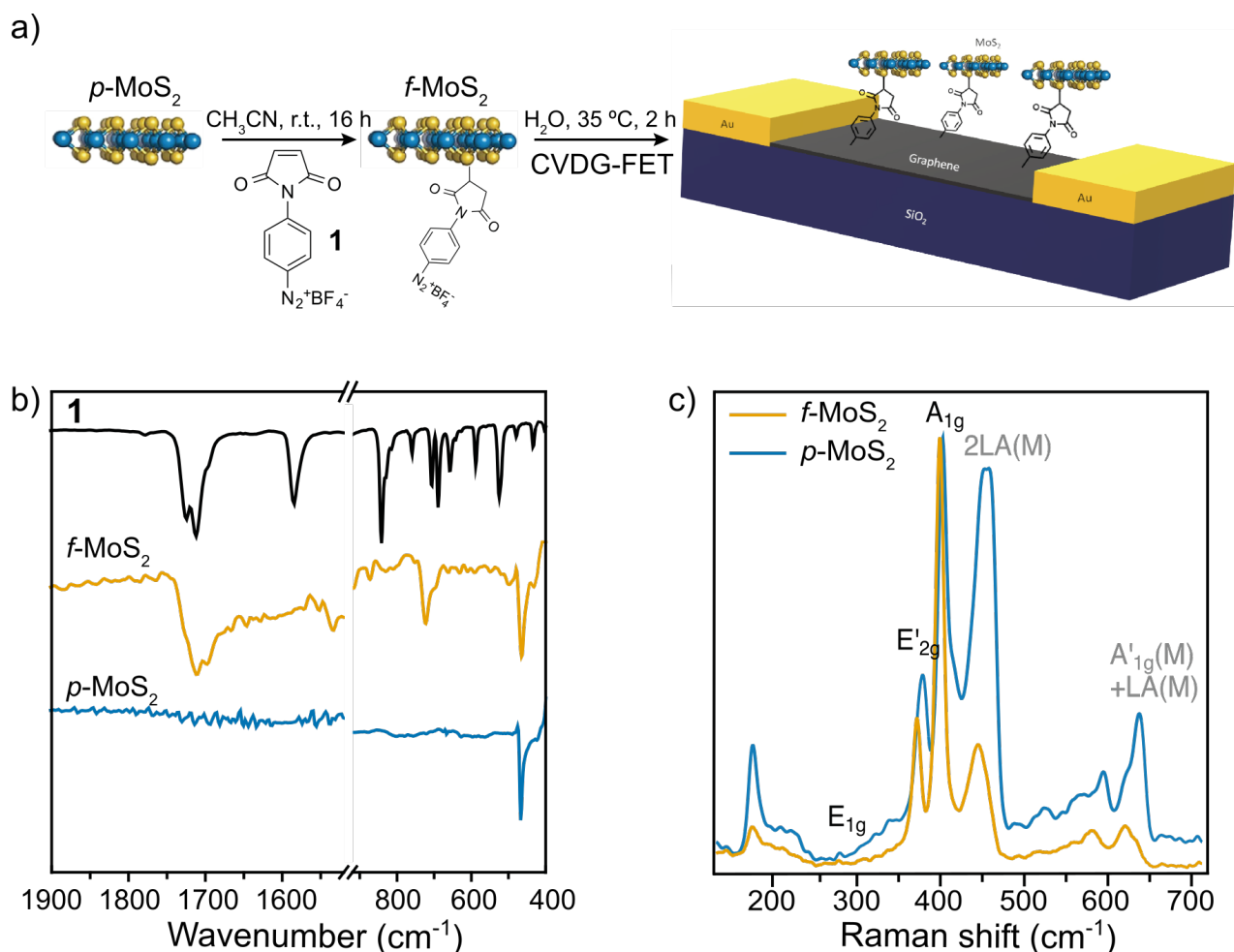


Figure 1. a) Scheme of the formation of the covalent heterostructure. Firstly, the covalent functionalization of exfoliated MoS₂ (*p*-MoS₂) with phenylmaleimide diazonium **1**. Secondly, the anchoring of *f*-MoS₂ onto CVD Graphene FET device (*f*-MoS₂/CVDG). b) FTIR spectra of **1** (black trace), *f*-MoS₂ (orange trace), *p*-MoS₂ (blue trace). c) Raman spectra ($\lambda_{\text{exc}} = 633 \text{ nm}$) of *f*-MoS₂ and *p*-MoS₂.

Formation and characterization of the covalent heterostructure

The covalent functionalization of the maleimide onto the surface of MoS₂ with a diazonium group makes the *f*-MoS₂ a suitable material for grafting onto carbon-based materials^{36,37}. To create the covalent heterostructure, a Si/SiO₂ substrate containing single-layer CVD-grown graphene (CVDG) was introduced in a suspension of *f*-MoS₂ in water at 35 °C. In order to avoid undesired precipitation of the sulfur material onto the surface, the substrate was positioned vertically. After reaction, the device was washed meticulously with water. As previously mentioned, fluorine atoms were not present in the pristine material, while the *f*-MoS₂ showed quantifiable amounts of it. Evidence of the decomposition of the diazo group and its consequent reactivity after the generation of the radical was found in the residues of the heterostructure reaction. The residual dispersion was filtered after reaction and XPS analysis showed the total disappearance of fluorine atoms from the MoS₂ surface (Supplementary Fig. 14).

To confirm the covalent anchoring of the MoS₂ flakes, Raman spectroscopy was performed to track the transformation of sp² carbon atoms of the graphene to sp³ as indication of formation of a new C-C bond. Figure 2a shows a statistical analysis of I_D/I_G band ratio over hundreds of points where MoS₂ flakes were found, observing a substantial increase of the I_D/I_G ratio from 0.05 ± 0.03 in the pristine CVDG to 0.13 ± 0.05 in the case of the covalent *f*-MoS₂/CVDG heterostructure. Besides, a 2D mapping of a representative graphene region (21 x 24 μm) where I_D/I_G ratio was analyzed in the same area, before (Supplementary Fig. 15) and after (Figure 2b) the reaction, showed a clear increase of the relative D band intensity in localized areas. The areas where the D band increases also show the presence of the $I_{A_{1g}}$ signals of the MoS₂ (Figure 2c), corroborating the formation of the covalent *f*-MoS₂/CVDG heterostructure.

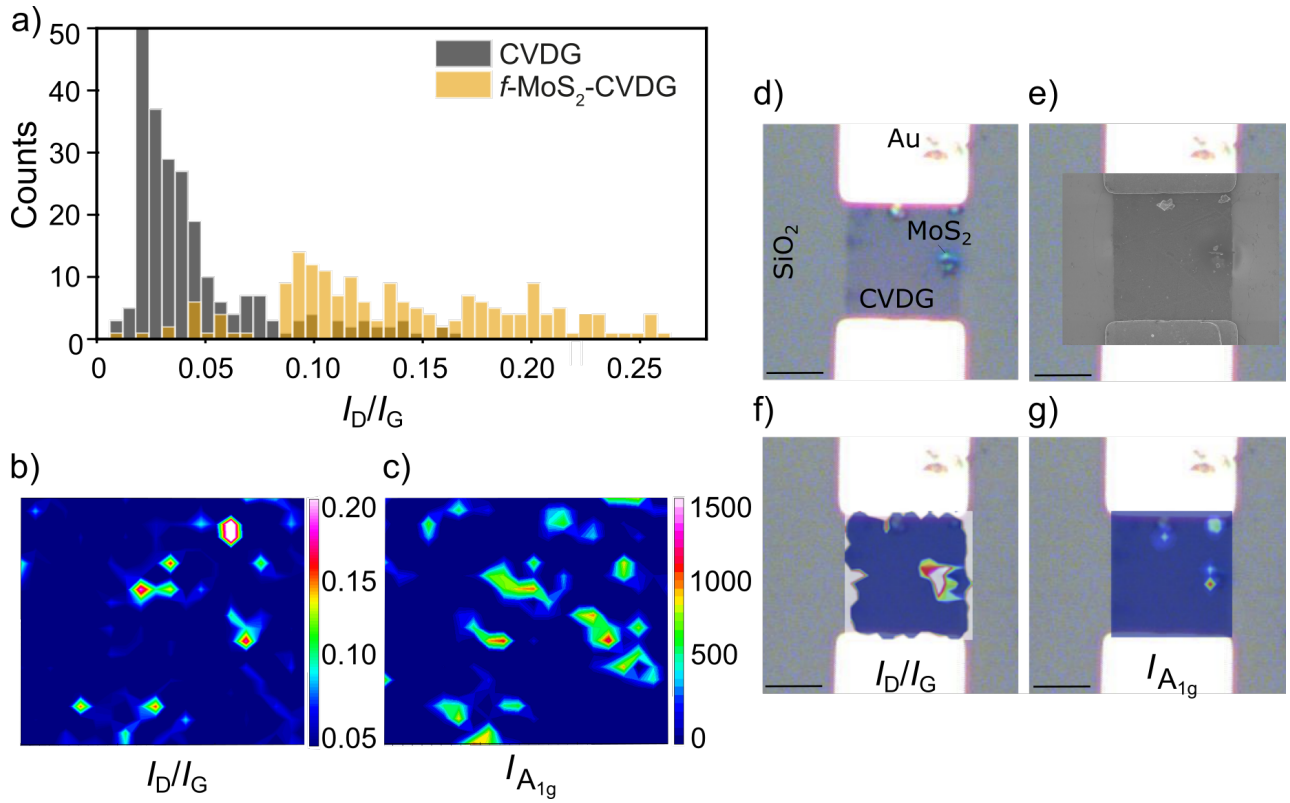


Figure 2. a) Histogram of the relative Raman intensities (I_D/I_G) of CVDG (before the reaction) and of f -MoS₂/CVDG heterostructure (λ_{exc} 532 nm, $N = >175$). b) I_D/I_G (λ_{exc} 532 nm) and c) $I_{A_{1g}}$ of MoS₂ (λ_{exc} 532 nm) 2D Raman mapping of a 21 x 24 μm area of f -MoS₂/CVDG heterostructure. d) Optical image and e) SEM of the covalent heterostructure f -MoS₂/CVDG FET device. Raman mapping with the relative intensities of I_D/I_G (f) and the MoS₂ $I_{A_{1g}}$ (g). The bright spots show the increase of the intensities at the same positions confirming the covalent anchoring of MoS₂. Scale bars of 5 μm .

Electrical properties

In order to measure the electrical properties of the heterostructure, we have fabricated graphene field-effect transistors (FET) on Si/SiO₂ substrates. In short, Cr/Au source and drain pads are deposited on CVD graphene by mask-less optical lithography and subsequent electron-beam evaporation of metals. In a second lithography step, we expose sets of 10x10 μm and 5x5 μm graphene bridges between the electrodes by optical lithography. The non-exposed graphene is removed by oxygen plasma etching. The devices are finally annealed at 300 $^{\circ}\text{C}$ for 8 hours to remove any remnant organic compounds

from the fabrication. Additional details about the fabrication process are described in the Supplementary information section. Supplementary Fig. 16 shows an optical and AFM image taken on a representative 10x10 μm -bridge device. The Raman spectra measured on different spots of the device show a low D band, indicative of a mostly defect-free graphene bridge before functionalization.

In a first functionalization step, a substrate containing tens of CVDG FETs was immersed in the *f*-MoS₂ water dispersion for two hours using the same reaction conditions already described, as previously mentioned. The devices were thereafter blown dried with nitrogen. After the reaction, a full characterization of the in situ generated *f*-MoS₂/CVDG FET can be observed in the Figure 2d-g. Optical microscopy showed the presence of bright flakes onto the surface of the graphene device. Raman mapping of the device with the relative intensities of I_D/I_G from graphene and $I_{A_{1g}}$ from the MoS₂ ratifies the covalent anchor of the flakes, caused by the fact that, as mentioned above, the increase in the I_D/I_G is observed where the MoS₂ flakes are located. Moreover, these results are in good agreement with SEM microscopy (Supplementary Fig. 17), where the preference of the *f*-MoS₂ flakes to anchor onto the CVDG device instead of the SiO₂ substrate can be clearly observed, together with some residual attachment to the gold electrode³⁸. A control experiment with pristine MoS₂, without chemical modification was carried out placing the suspension of MoS₂ on top of the graphene, observing no significant changes in the D band intensity.

Further evidence of the covalent functionalization is observed in electron transport measurements. Gate voltage characteristics (I_{sd} - V_g) are measured on the CVDG FETs before and after the functionalization with *f*-MoS₂. The Si substrate serves as back-gate electrode and the SiO₂ as dielectric insulator. All the measurements were performed under vacuum conditions ($\sim 10^{-6}$ mbar) unless otherwise specified. In pristine CVDG devices, the typical Dirac cone of semi-metallic graphene appears centred at $V_g = 35.5$ V, as shown in Figure 3a (black trace). In addition, the cone is clearly asymmetric with significantly lower mobility for negative charge carriers. See Supplementary

Fig. 18 for the full gate voltage window. Graphene is therefore initially p-doped by electron-withdrawer impurities, most likely as a consequence of remnant adsorbates from the fabrication process, the CVD growth or charged impurities in the SiO_2 substrate, as described in the literature^{25,39,40}.

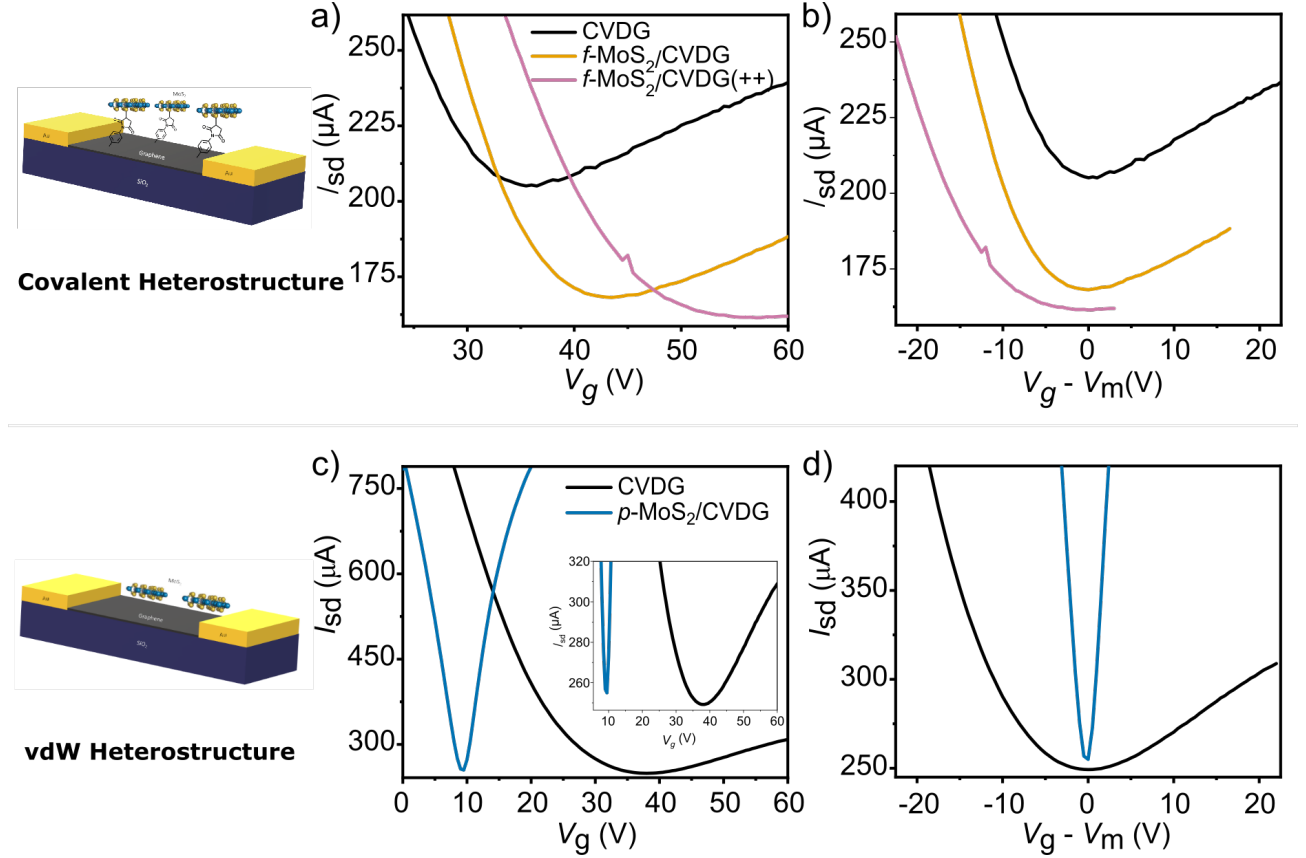


Figure 3. a) Gate voltage characteristics (I_{sd} - V_g) measured on a CVDG-FET (black trace), the same device after two hours functionalization with $f\text{-MoS}_2$ (orange), and additional two hours functionalization (pink). b) The same gate voltage characteristics renormalized to the V_g potential at the cone minimum V_m . c) Gate voltage characteristics (I_{sd} - V_g) measured on a pristine graphene FET (black) and the same device after generating the vdW heterostructure (blue). The inset is a closer view of the cone minimum area. d) The same gate voltage characteristics renormalized to the V_g potential at the cone minimum V_m .

The gate trace measured in the $f\text{-MoS}_2\text{-CVDG}$ FET (orange curve in Figure 3a) reveals a shift of the Dirac cone towards positive gate voltages ($V_g = 43.5$ V) after the functionalization. This could be due

to an electron withdrawal mechanism during the formation of the aryl covalent bond⁴¹ but also due to charge transfer from the diazonium molecules when physisorbed on graphene^{25,42}. The diazonium molecule has a well-known electron-withdrawer nature^{25,41,42}. Indeed, it could be expected that only a fraction of the diazonium molecules covalently bond to the MoS₂ flakes will participate in the covalent formation of the heterostructure with graphene. In particular, reactivity will be locally higher for those linkers close to corrugated regions in graphene,⁴² the edges or grain boundaries and n-doped puddles²⁵.

Interestingly, the shift of the Dirac cone is accompanied by a clear reduction of the current at the cone minimum (18% reduction), together with a broadening of the cone minimum. This trend is clearer in Figure 3b where the gate traces have been renormalized to the potential at the cone minimum ($V_g - V_m$). The current suppression in graphene is unambiguously associated to the disruption of the sp^2 hybridization into a sp^3 hybridization due to the formation of covalent bonds^{41,43}, in this case between the diazonium molecule and the graphene. This finding is consistent with the increment of the D band observed in the Raman measurements that also points to the formation of covalent bonds, as showed in Figure 2.

A second functionalization of the same device during two additional hours (pink curve in Figure 3) yields a further shift of the Dirac cone towards positive gate voltages ($V_g = 57$ V). The current at the cone minimum is further suppressed but in a lesser relative degree (4% reduction). This seems to indicate that the initial two hours functionalization is enough to promote covalent bonding in most of the available graphene spots with higher reactivity. Note that the control samples where the devices are exposed to only the DI water solvent show no significant doping effect on graphene after annealing (see Supplementary Fig. 21). Interestingly, the charge carrier mobility does not change significantly after functionalization and covalent bond formation between *f*-MoS₂ and graphene. The hole mobility in the sample in Figure 3a stays around $\mu_h = 500 \text{ cm}^2\text{V}^{-1}\text{s}^{-1}$ before and after the second *f*-MoS₂ functionalization. It actually slightly increases after the first functionalization, most likely as

a consequence of the interaction with MoS₂, as seen in the Supplementary Materials and has been previously reported⁴⁴. Electron mobility is $\mu_e = 66 \text{ cm}^2\text{V}^{-1}\text{s}^{-1}$ for pristine graphene and lays out of the gate window for functionalized devices. See supporting information for additional details. The same trend appears in 19 out of 22 (86 %) measured devices (see Supplementary Fig. 19 for additional examples). The degree of p-doping and suppression of the current at the minimum, and therefore the possible chemisorption/physisorption balance, shows minor fluctuations from device to device. See Supplementary Fig. 20 for detailed statistics.

The emergence of a p-doping effect on graphene in the covalent heterostructure seems to indicate that the electron-withdrawing character of the linker is predominant over the typically electron-donor character of MoS₂ when combined with graphene. It could also indicate that the diazonium linker acts as electronic spacer between graphene and MoS₂. To better understand the role of the two components, we have studied separately the effect of the bare MoS₂ flakes and the bare diazonium salt used as linker when they couple to graphene. Supplementary Fig. 22 shows the gate voltage characteristic of a representative device after dipping the substrate with the diazonium salt **1** for two hours. A substantially stronger p-doping effect and pronounced reduction of the hole mobility on graphene in comparison with the covalent heterostructure is observed. On the other hand, Figure 3c and d shows the gate trace of a representative pristine graphene FET and the same device after drop casting in DI water containing bare MoS₂ flakes (without diazonium linkers). Four main fingerprints of the van der Waals heterostructure appear that are not observed in the covalent heterostructures. First, a clear shift to lower gate voltages indicates n-doping of graphene as a consequence of the interactions with MoS₂. Second, the mobility of the electron charge carriers increases. Third, the current at the cone minimum slightly increases. Finally, the cone at the tip becomes sharper. This trend is observed in 12 of 13 (92%) measured devices. The electron properties of the *f*-MoS₂/CVDG device system seems therefore to be the final balance from the competition between diazonium molecules and MoS₂.

Finally, we carried out preliminary photoresponsivity experiments by shining the heterostructure with an ultraviolet laser source (365 nm). The initial characterization shows a photoresponse similar to the one described for graphene/MoS₂ van der Waals heterostructures (Supplementary Fig. 23)⁴⁵. The photoelectric properties are therefore preserved in this covalent analogue. Further studies will be necessary to understand the role of other dopants, light intensity and wavelength in the photoresponsivity of the covalent heterostructure.

CONCLUSION

In conclusion, we show how to use the tools of chemistry to interface MoS₂ and graphene. In particular, we use chemoselectivity concepts to design a bifunctional molecule with a maleimide group, reactive towards MoS₂ under mild nonaqueous conditions, and a diazonium derivative, that is activated in water towards reaction with graphene. We use this to connect MoS₂ flakes to several graphene FET devices simultaneously. We observe that the electronic properties of the functionalized devices are dominated by the chemical interface, resulting in p-doped devices in which the charge mobility is conserved after reaction, and the degree of doping can be controlled by increasing the degree of functionalization. Very recently, Samorí and co-workers have shown the potential of chemistry to improve the performance devices based on a single TMDC through covalent connection⁴⁶. The results described here show the power of the chemical approach to build functional 2D-2D heterostructures beyond van der Waals⁴⁷. In particular, vertical covalent connection brings an additional lever on the final properties of devices, beyond the intrinsic properties of the materials, and has the potential for facile high-throughput homologation.

Methods

Preparation of Liquid Phase Exfoliation MoS₂ (p-MoS₂). Liquid-Phase Exfoliation of MoS₂: 200 mg of MoS₂ powder and 200 mL of NMP were added in a round-bottom flask. The mixture was sonicated in a Vibracell 75115 (VC 505 / VC 750)-Bioshock Scientific. The Ultrasonic Processor was used

during an hour, operating at the amplitude of 37%, without pulse at 2 °C. Afterwards, the black dispersion was centrifuged for 30 minutes at 5000 rpm (Allegra X-15R Beckman Coulter centrifuge, FX6100 rotor, 20 °C). Then, the supernatant (olive-color) was separated from the black sediment (non-exfoliated) by decanting and filtering with Omnipore 0.45 µm PTFE membrane filters, 45 mm in diameter. The membrane with the retained exfoliated MoS₂ was dispersed in acetonitrile and filtered again in order to clean the material. This re-dispersion process was repeated three times with 60 mL of acetonitrile and three times with 60 mL of isopropanol.

Functionalization of p-MoS₂ with N-(4-diazophenyl)maleimide. A 0.4 mg/mL dispersion of exfoliated MoS₂ is prepared by 10 seconds sonication of 8 mg of the material and 20 mL of dry acetonitrile in a glass vial. 1 mmol of N-(4-diazophenyl)maleimide is added to the dispersion and the mixture is stirred 16 hours at room temperature protected from the light. The resulting material is filtered with Omnipore 0.45 µm PTFE membrane filters (diameter of 25 mm) and washed three times with 40 mL of acetonitrile

Also, the first washing was concentrated under vacuum and the solid obtained was characterized by NMR, to prove that the starting maleimide derivative was not altered during the reaction, and the diazonium group is not affected. NMR spectrum obtained is identical to the reagent.

Preparation of f-MoS₂/CVDG heterostructure. 1 mg of f-MoS₂ was dispersed in 10 mL of DI H₂O using a sonication bath for 10 minutes. Then CVDG-FET was vertically submerged held for 2h at 35 °C in the absence of light. The resulting f-MoS₂/CVDG device was carefully washed with DI H₂O and flushed under N₂ flow. Same procedure was used for the f-MoS₂/CVDG FET heterostructure.

Acknowledgements

The authors acknowledge European Research Council (ERC-PoC- 842606 ; ERC-AdG-742684), MINECO (CTQ2017-86060-P and CTQ2016-79419-R), Ministerio de Ciencia e Innovación (RTI2018-096075-A-C22) the Comunidad de Madrid (MAD2D-CM S2013/ MIT-3007,

Y2018/NMT-4783 and the Programa de Atracción del Talento Investigador 2017-T1/IND-5562). CzechNanoLab Research Infrastructure supported by MEYS CR (LM2018110) are gratefully acknowledged. IMDEA Nanociencia acknowledges support from the “Severo Ochoa” Programme for Centres of Excellence in R&D (MINECO, Grant SEV- 2016-0686).

Author Contributions

M.V.S., E.B. and E.M.P. conceived and designed experiments. M.V.S., R.Q.O. and M.V.H. synthesized compound **1**. M.V.S. and R.Q.O. exfoliated and functionalized the materials. M.V.S., R.Q.O., N.M.S. and I.J.G. carried out the chemical and structural characterization. A.D. and E.B. fabricated the nanodevices and performed the electrical measurements. V.S., J. S., E.B., and E.M.P. supervised research and directed data analysis. M.V.S., E.B. and E.M.P. wrote the manuscript, with contributions from all authors.

Competing Interests statement

The authors declare no competing interests.

References

- 1 Liu, Y. et al. Van der Waals heterostructures and devices. *Nat Rev. Mater.* **1**, 16042, (2016).
- 2 Robinson, J. A. Growing Vertical in the Flatland. *ACS Nano* **10**, 42-45, (2016).
- 3 Geim, A. K. & Grigorieva, I. V. Van der Waals heterostructures. *Nature* **499**, 419-425, (2013).
- 4 Yankowitz, M., Ma, Q., Jarillo-Herrero, P. & LeRoy, B. J. van der Waals heterostructures combining graphene and hexagonal boron nitride. *Nat. Rev. Phys.*, **1**, 112-125, (2019).
- 5 Neupane, G. P. et al. In-Plane Isotropic/Anisotropic 2D van der Waals Heterostructures for Future Devices. *Small* **15**, e1804733, (2019).
- 6 Novoselov, K. S., Mishchenko, A., Carvalho, A. & Castro Neto, A. H. 2D materials and van der Waals heterostructures. *Science* **353**, aac9439, (2016).
- 7 Jariwala, D., Marks, T. J. & Hersam, M. C. Mixed-dimensional van der Waals heterostructures. *Nat. Mater.* **16**, 170-181, (2017).
- 8 Bertolazzi, S., Krasnozhan, D. & Kis, A. Nonvolatile memory cells based on MoS₂/graphene heterostructures. *ACS Nano* **7**, 3246-3252, (2013).
- 9 Ulstrup, S. et al. Ultrafast Band Structure Control of a Two-Dimensional Heterostructure. *ACS Nano* **10**, 6315-6322, (2016).
- 10 Shi, Y. et al. van der Waals epitaxy of MoS₂ layers using graphene as growth templates. *Nano Lett.* **12**, 2784-2791, (2012).
- 11 Yu, L. et al. Graphene/MoS₂ hybrid technology for large-scale two-dimensional electronics. *Nano Lett.* **14**, 3055-3063, (2014).

- 12 Lorchat, E. et al. Filtering the photoluminescence spectra of atomically thin semiconductors with graphene. *Nat. Nanotechnol.* **15**, 283-288, (2020).
- 13 Wang, X. et al. Realization of vertical metal semiconductor heterostructures via solution phase epitaxy. *Nat. Commun.* **9**, 3611, (2018).
- 14 Le, C. T. et al. Effects of Interlayer Coupling and Band Offset on Second Harmonic Generation in Vertical MoS₂/MoS₂(1-x)Se_{2x} Structures. *ACS Nano* **14**, 4366-4373, (2020).
- 15 Choi, W. et al. Optoelectronics of Multijunction Heterostructures of Transition Metal Dichalcogenides. *Nano Lett.* **20**, 1934-1943, (2020).
- 16 Li, C. et al. Engineering graphene and TMDs based van der Waals heterostructures for photovoltaic and photoelectrochemical solar energy conversion. *Chem. Soc. Rev.* **47**, 4981-5037, (2018).
- 17 Duong, D. L., Yun, S. J. & Lee, Y. H. van der Waals Layered Materials: Opportunities and Challenges. *ACS Nano* **11**, 11803-11830, (2017).
- 18 Vera-Hidalgo, M., Giovanelli, E., Navio, C. & Perez, E. M. Mild Covalent Functionalization of Transition Metal Dichalcogenides with Maleimides: A "Click" Reaction for 2H-MoS₂ and WS₂. *J. Am. Chem. Soc.* **141**, 3767-3771, (2019).
- 19 Quirós-Ovies, R. et al. Controlled Covalent Functionalization of 2H-MoS₂ with Molecular or Polymeric Adlayers. *Chem. Eur. J.* **26**, 6629-6634 (2020).
- 20 Vázquez Sulleiro, M. et al. Covalent Cross-Linking of 2H-MoS₂ Nanosheets. *Chem. Eur. J.* **27**, 2993-2996, (2021).
- 21 Villalva, J. et al. Covalent modification of frambolite with maleimides: connecting molecules and van der Waals heterostructures. *Nanoscale Horiz.* **n/a**, (2021).
- 22 Bahr, J. L. & Tour, J. M. Highly functionalized carbon nanotubes using in situ generated diazonium compounds. *Chem. Mater.* **13**, 3823-3824, (2001).
- 23 Strano, M. S. et al. Electronic structure control of single-walled carbon nanotube functionalization. *Science* **301**, 1519-1522, (2003).
- 24 Bahr, J. L. et al. Functionalization of carbon nanotubes by electrochemical reduction of aryl diazonium salts: a bucky paper electrode. *J. Am. Chem. Soc.* **123**, 6536-6542, (2001).
- 25 Paulus, G. L., Wang, Q. H. & Strano, M. S. Covalent electron transfer chemistry of graphene with diazonium salts. *Acc. Chem. Res.* **46**, 160-170, (2013).
- 26 Lomeda, J. R. et al. Diazonium Functionalization of Surfactant-Wrapped Chemically Converted Graphene Sheets. *J. Am. Chem. Soc.* **130**, 16201-16206, (2008).
- 27 Liu, Y., Zhao, Y., Jiao, L. & Chen, J. A graphene-like MoS₂/graphene nanocomposite as a highperformance anode for lithium ion batteries. *J. Mater. Chem. A* **2**, 13109-13115, (2014).
- 28 Mahouche-Chergui, S., Gam-Derouich, S., Mangeney, C. & Chehimi, M. M. Aryl diazonium salts: a new class of coupling agents for bonding polymers, biomacromolecules and nanoparticles to surfaces. *Chem. Soc. Rev.* **40**, 4143-4166, (2011).
- 29 Boukerma, K., Chehimi, M. M., Pinson, J. & Blomfield, C. X-ray photoelectron spectroscopy evidence for the covalent bond between an iron surface and aryl groups attached by the electrochemical reduction of diazonium salts. *Langmuir* **19**, 6333-6335, (2003).
- 30 Lomeda, J. R. et al. Diazonium functionalization of surfactant-wrapped chemically converted graphene sheets. *J. Am. Chem. Soc.* **130**, 16201-16206, (2008).
- 31 Benson, E. E. et al. Balancing the hydrogen evolution reaction, surface energetics, and stability of metallic MoS₂ nanosheets via covalent functionalization. *J. Am. Chem. Soc.* **140**, 441-450, (2018).
- 32 Chen, X. et al. Covalent Bisfunctionalization of Two-Dimensional Molybdenum Disulfide. *Angew. Chem. Int. Ed.* **n/a**, (2021).
- 33 Fan, J.-H. et al. Resonance Raman scattering in bulk 2H-MX₂ (M= Mo, W; X= S, Se) and monolayer MoS₂. *J. Appl. Phys.* **115**, 053527, (2014).

- 34 Knirsch, K. C. et al. Basal-Plane Functionalization of Chemically Exfoliated Molybdenum Disulfide by Diazonium Salts. *ACS Nano* **9**, 6018-6030, (2015).
- 35 Mignuzzi, S. et al. Effect of disorder on Raman scattering of single-layer MoS₂. *Phys. Rev. B* **91**, 195411, (2015).
- 36 Assresahegn, B. D., Brousse, T. & Bélanger, D. Advances on the use of diazonium chemistry for functionalization of materials used in energy storage systems. *Carbon* **92**, 362-381, (2015).
- 37 Bahr, J. L. & Tour, J. M. Highly functionalized carbon nanotubes using in situ generated diazonium compounds. *Chem. Mater.* **13**, 3823-3824, (2001).
- 38 Wang, Y. et al. Photoelectrochemical immunosensing of tetrabromobisphenol A based on the enhanced effect of dodecahedral gold nanocrystals/MoS₂ nanosheets. *Sens. and Actuators B* **245**, 205-212, (2017).
- 39 Ryu, S. et al. Atmospheric oxygen binding and hole doping in deformed graphene on a SiO₂ substrate. *Nano Lett.* **10**, 4944-4951, (2010).
- 40 Wang, Q. H. et al. Understanding and controlling the substrate effect on graphene electron-transfer chemistry via reactivity imprint lithography. *Nat. Chem.* **4**, 724-732, (2012).
- 41 Fan, X. Y., Nouchi, R., Yin, L. C. & Tanigaki, K. Effects of electron-transfer chemical modification on the electrical characteristics of graphene. *Nanotechnology* **21**, 475208, (2010).
- 42 Farmer, D. B. et al. Chemical doping and electron–hole conduction asymmetry in graphene devices. *Nano Lett.* **9**, 388-392, (2009).
- 43 Sinitskii, A. et al. Kinetics of diazonium functionalization of chemically converted graphene nanoribbons. *ACS Nano* **4**, 1949-1954, (2010).
- 44 Pham, T. et al. MoS₂-graphene heterostructures as efficient organic compounds sensing 2D materials. *Carbon* **142**, 504-512, (2019).
- 45 Zhang, W. et al. Ultrahigh-gain photodetectors based on atomically thin graphene-MoS₂ heterostructures. *Sci. Rep.* **4**, 3826, (2014).
- 46 Ippolito, S., et al. Covalently interconnected transition metal dichalcogenide networks via defect engineering for high-performance electronic devices. *Nat. Nanotechnol.* **16**, 592–598 (2021).
- 47 Gbadamasi, S. et al. Interface chemistry of two-dimensional heterostructures—fundamentals to applications. *Chem. Soc. Rev.* **50**, 4684-4729 (2021).

Supplementary Information

1. Experimental procedures

Characterization and instrumentation

UV-Vis spectroscopy was recorded on a Cary 50 UV-Visible spectrophotometer employing dispersions of the 2D material in acetonitrile and quartz cuvettes. Each suspension was sonicated and transferred into a quartz cuvette (path length = 1 cm). The cuvette was closed with a lid and the extinction spectra of the samples were measured immediately (time zero measurement).

Raman spectroscopy was carried out on a Senterra Raman Spectrometer confocal Raman microscope (Bruker Optic, Ettlingen, Germany, resolution 3-5 cm⁻¹). Powder samples were dried and supported onto precleaned glass slides and pressure was applied to attach the material, remaining a perfectly flat surface. The parameters used were 633 nm excitation laser, 2 mW; scanning: 1'' acquisition, 2 coadditions; objective NA 0.75, 50X, > 30 points on random areas. CVDG and *f*-MoS₂/CVDG devices were measured using 532 nm laser excitation, 2 mW; scanning: 1'', 3 coadditions; objective NA 0.75, 50X. Statistical analysis of the heterostructure (*f*-MoS₂/CVDG), (>170 points) were counted only where MoS₂ signals were observed. Mappings measurements have an area greater than 400 μm² (specified in the figure caption), mappings of field effect transistors cover the entire area of the device. For SERS experiments, the solid sample/pristine and functionalized flakes were diluted in acetonitrile, sonicated for 10 min and deposited by drop casting on commercial Au SERS substrates (Silmecc). The purchased substrates are composed by a nanostructured Si substrate coated with a thin Au film. The parameters used were 50X objective, 633 nm wavelength, 0.2 mW, 1'' acquisition.

NMR was performed on a BrukerAvance 400 at 298 K using the corresponding deuterated solvent noted. Chemical shifts (δ) are denoted in ppm.

Thermogravimetric Analysis (TGA) was carried out in a TA Q500 instrument. The experiments were running out under air flow, using a temperature ramp of 10 °C/min from 100 to 1000 °C.

Fourier-transform infrared spectroscopy with attenuated total reflection (FT-ATR-IR) was performed in a Bruker ALPHA FT-IR spectrometer.

Atomic force microscopy (AFM) images were acquired using a commercial AFM system (Ntegra Prima) in semicontact (dynamic) mode using scanning by sample configuration in ambient conditions. Rectangular silicon cantilevers HA_NC (NT-MDT) were used with typical values of 5.1 N·m⁻¹ spring constant and 150 kHz resonant frequency. The resulting images were processed using Gwyddion software.

X-ray photoelectron spectroscopy (XPS) measurements were performed with an Axis Supra spectrometer (Kratos Analytical Ltd, UK). The samples were drop casted onto an Au substrate; spectra were acquired with a charge neutralization beam to avoid differential charging of samples. The quantitative composition was determined from detailed spectra taken at the pass energy of 80 eV. Lower pass energy of 20 eV was used to attain well-resolved spectra for fitting. The deconvolution of XPS spectra to individual components was done in the Casa XPS 2.3.17 software. For the fitting, the Shirley- type background subtraction was used, and all curves were defined as 30 % Lorentzian, 70 % Gaussian. Besides, constrains of the full width at a half maximum (FWHM) and the peak positions were applied. Binding energy calibration was based on adventitious carbon at 284.8 eV.

X-ray diffraction (XRD) measurements were carried out using a Panalytical X'Pert PRO theta/2theta diffractometer with Cu-K α radiation (λ = 0.1541 nm).

Scanning electron microscopy (SEM) of the devices were characterized working on a low voltage (1.5 kV) and current (10 pA) mode to avoid any damage of the sample by using a FESEM Auriga, Carl Zeiss.

Materials

All reagents were obtained from Sigma Aldrich, including MoS₂ powder (99%) and CVDG (on Cu and transferred to SiO₂).¹ Solvents were purchased from Scharlab Chemicals S. L. and used as received.

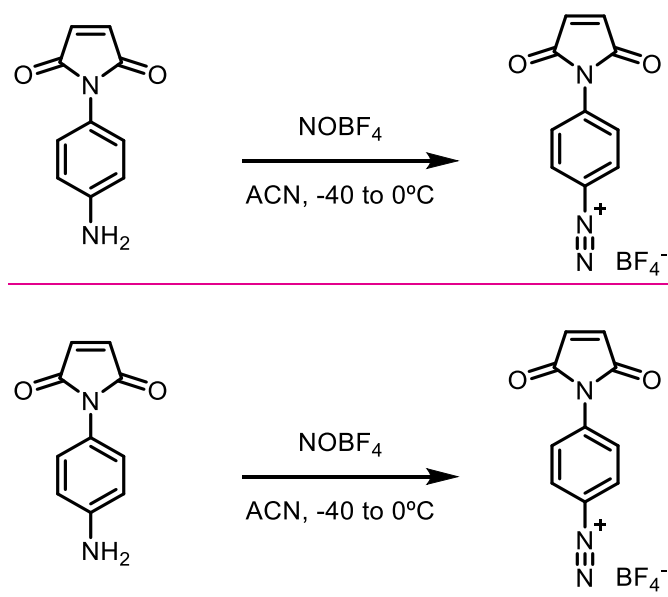
Preparation of the van der Waals heterostructure *p*-MoS₂/CVDG

1mg of *p*-MoS₂ was sonicated in 10 mL of DI H₂O using a sonication bath for 10 minutes. Then, 20 µL of the dispersion was dropped onto CVDG substrate for 30 minutes.

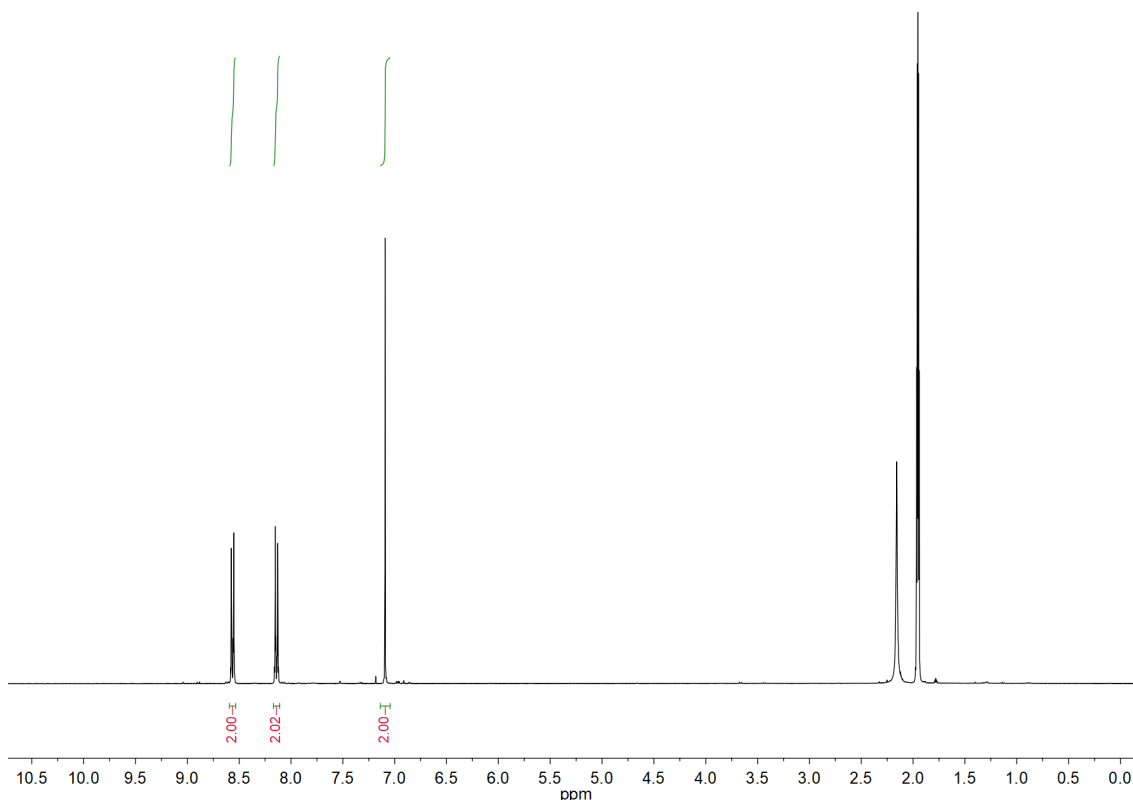
Functionalization of CVDG with *N*-(4-Diazophenyl)maleimide tetrafluoroborate (1**)**

CVDG was submerged in a solution 0.1 mM of **1** and DI H₂O (10mL) at 35 °C. After 2 h the substrate was washed several times with H₂O and flushed under N₂ flow. Raman spectroscopy confirmed the covalent functionalization of **1** with CVDG.

Synthesis of *N*-(4-Diazophenyl)maleimide tetrafluoroborate (1**)**



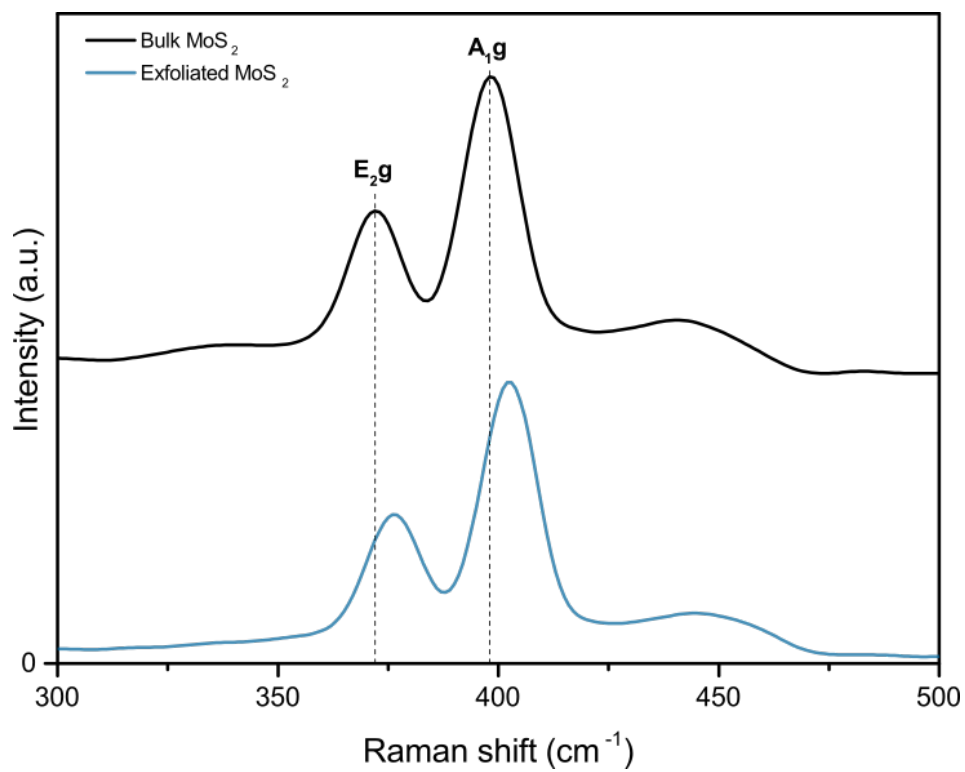
N-(4-Aminophenyl)maleimide (935 mg, 5 mmol, 1 eq.) and nitronium tetrafluoroborate (878 mg, 7.5 mmol, 1.5 eq.) were added to two different Schlenk flasks under argon atmosphere and each one was dissolved in 20 mL of dry acetonitrile. Both solutions were cooled to -40°C (dry ice in acetonitrile). Then, *N*-(4-Aminophenyl)maleimide was slowly cannulated into the second solution and the mixture was stirred for 1 hour at -40°C . After that, it was gradually allowed to warm up to 0°C for 2 hours. Finally, the resulting solution was poured into 500 mL of cool diethyl ether. The obtained yellow precipitate was filtered, washed three times with 50 mL of diethyl ether and dried under vacuum. ^1H NMR (400 MHz, CD_3CN) δ (ppm): 8.56 (d, 2H), 8.14 ppm (d, 2H), 7.09 ppm (s, 2H).



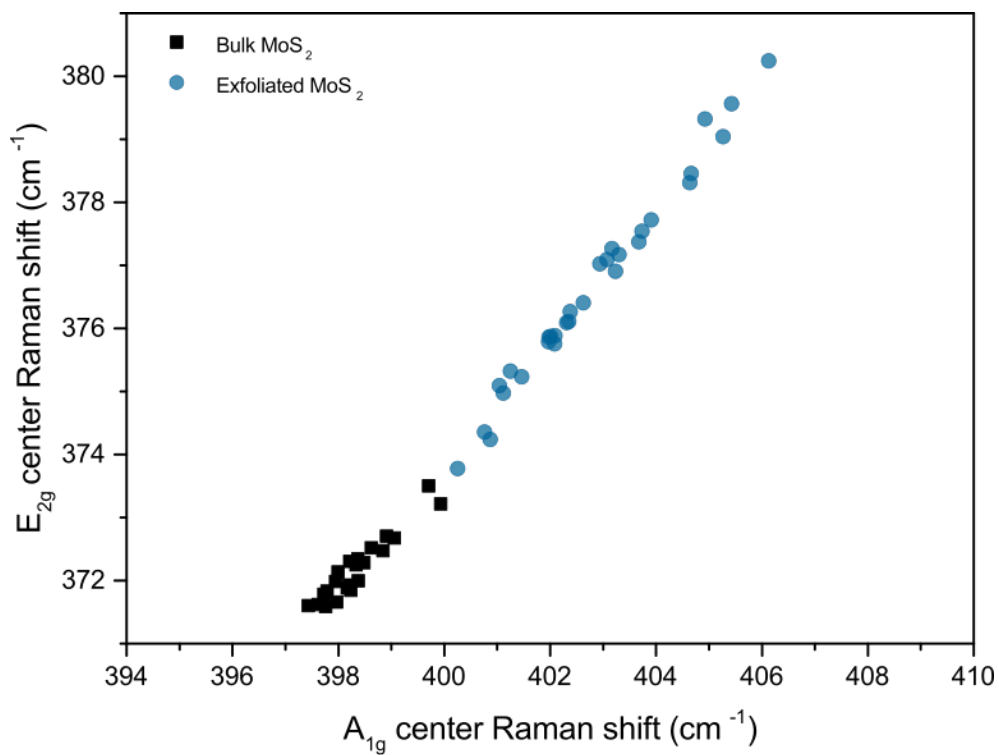
Fabrication of the field effect transistors

The fabrication of the graphene field-effect transistors involved two optical lithography steps. Initially, Si/SiO₂ wafers were cleaned using isopropanol and acetone to remove any traces of organic, ionic, and metallic impurities. Then, AZ1505 positive photoresist was spin coated at 5000 rpm for 1 min onto the surface followed by baking at 90°C for 1 min to form a 450 nm resist layer. The electrodes and pads were defined by exposing the surface to UV light using a Heidelberg Instruments DWL66fs laser writer of 405nm (h-line) with 300 mJ/cm² dose. The pattern is subsequently developed with AZ-351B. Thereafter 5nm Cr and 80nm Au layers were deposited using Ecovac e-beam evaporation by Angstrom Engineering. The source/drain electrodes are then obtained by lift-off. A second lithography step was carried out to etch graphene from unwanted areas and thus create a graphene channel between the electrodes. Negative photoresist AZ nLof 2070 was used to protect the graphene bridge between electrodes and the rest was exposed to oxygen plasma to etch. Finally, the resist was removed with acetone. Channel dimensions were set to 10x10μm and 5x5μm. The devices were annealed at 300°C for 8 hours after the fabrication.

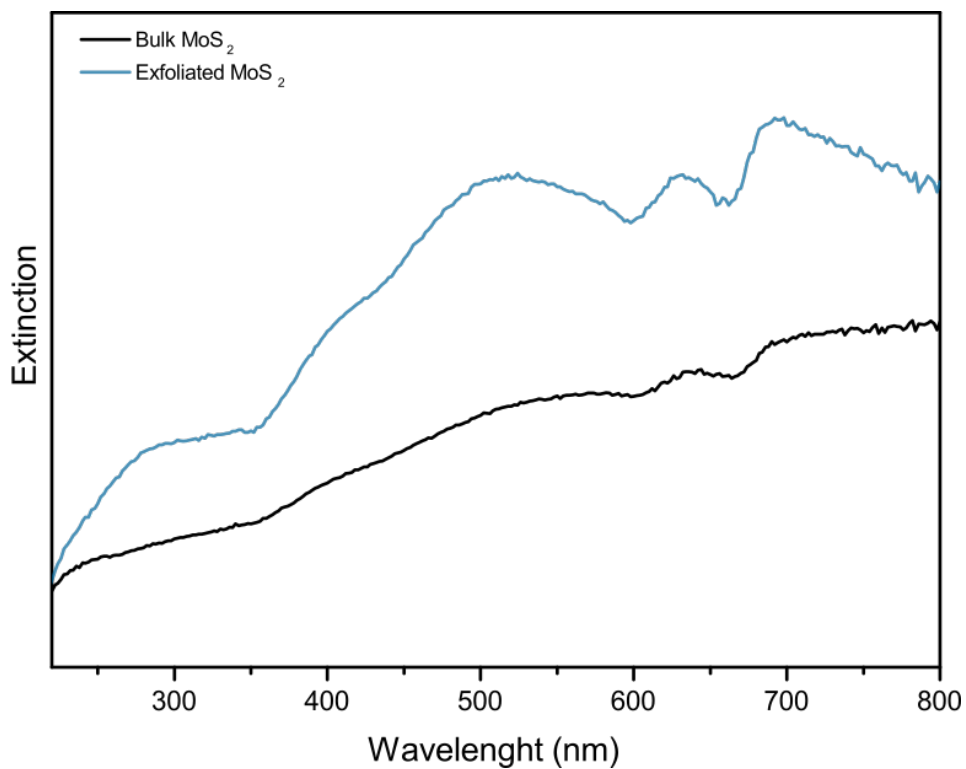
2. Characterization of p -MoS₂ and f -MoS₂



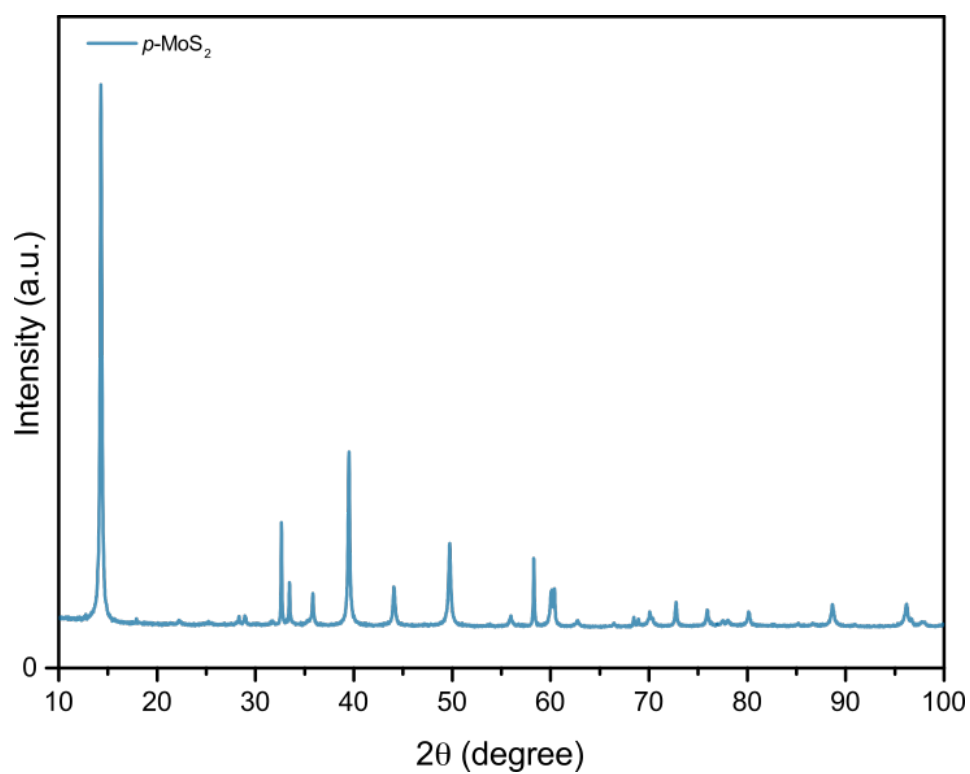
Supplementary Figure 1. Average (30 points) Raman spectra (λ_{exc} 532 nm) of Bulk material and liquid phase exfoliated material.



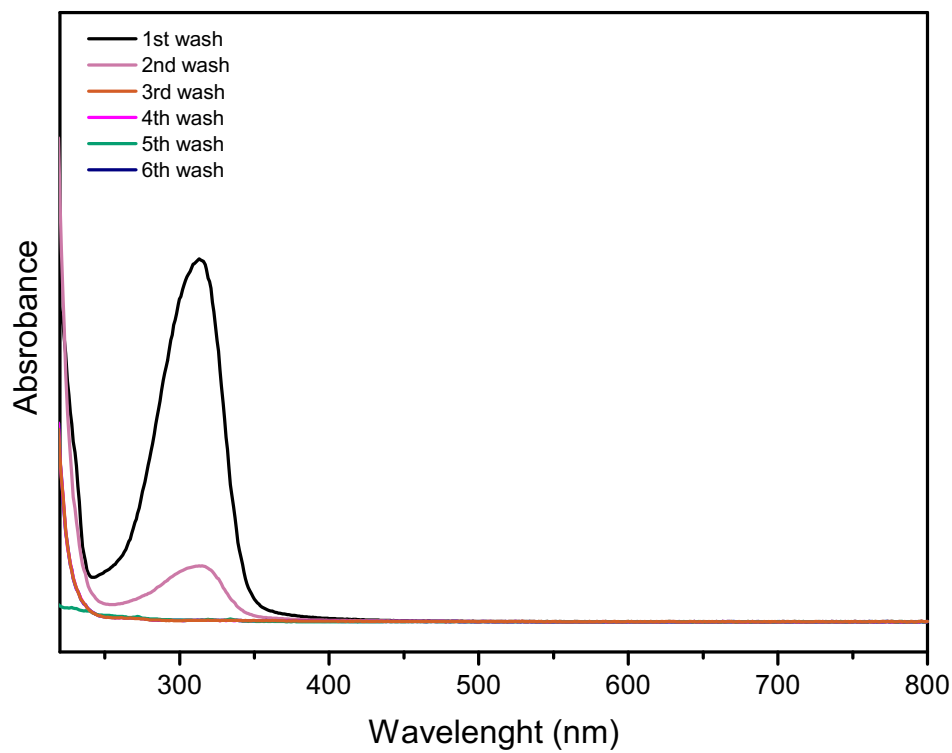
Supplementary Figure 2. Correlation plot of the E_{2g} , A_{1g} Raman peaks measured with 532 nm laser excitation.



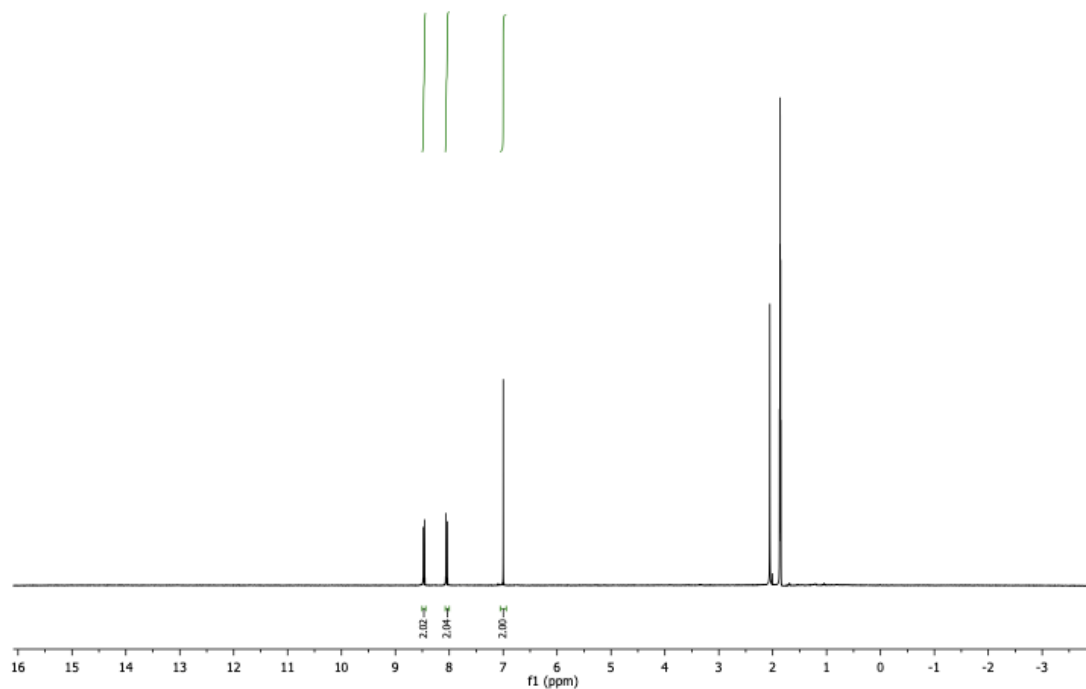
Supplementary Figure 3. UV-Vis spectroscopy of Bulk and exfoliated MoS₂ colloids (*p*-MoS₂).



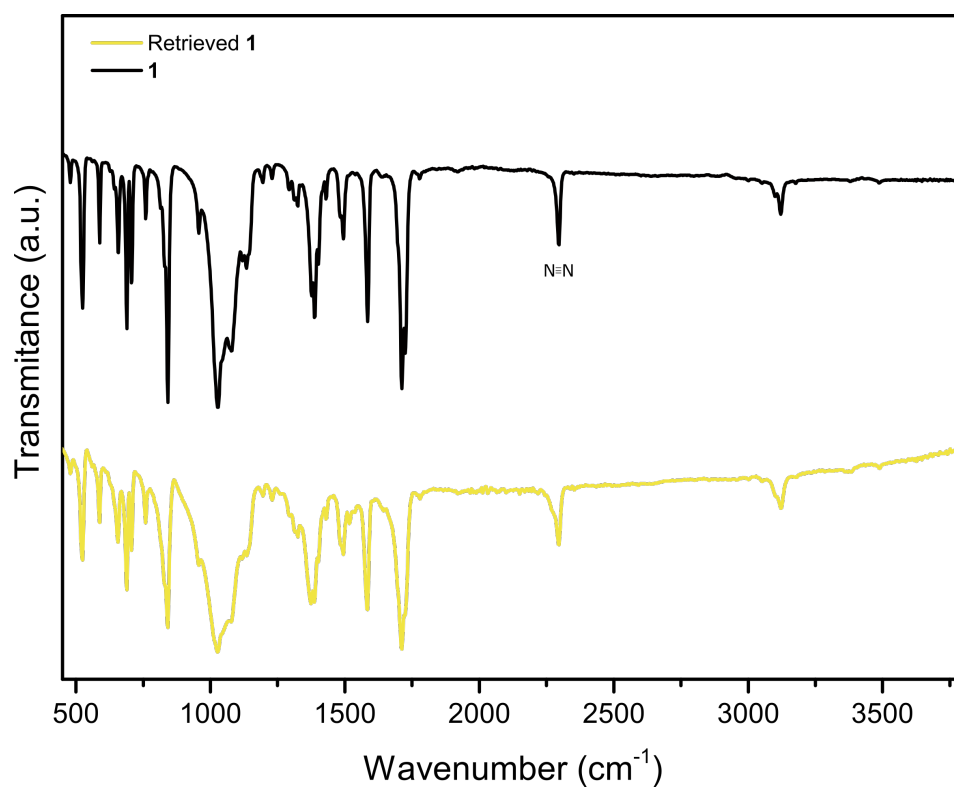
Supplementary Figure 4. XRD of exfoliated MoS_2 .



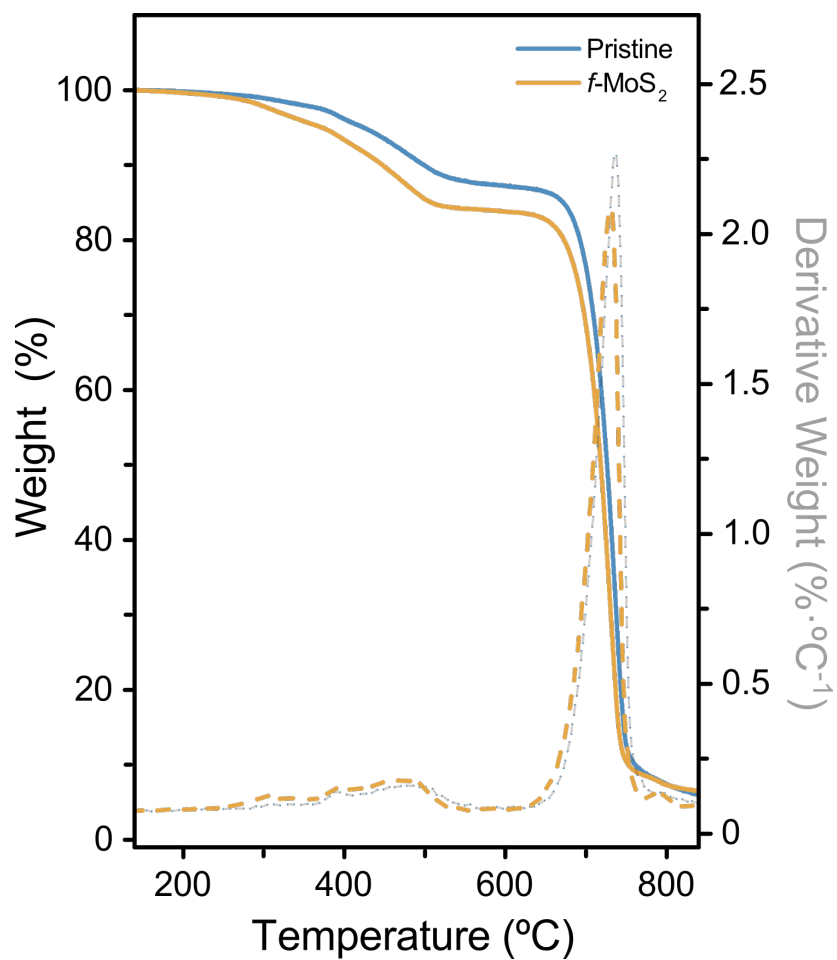
Supplementary Figure 5. UV-Vis spectra of different washes after the functionalization of MoS_2 .



Supplementary Figure 6. ^1H NMR spectrum (400 MHz CD_3CN) of **1** residue after collection from MoS_2 reaction.



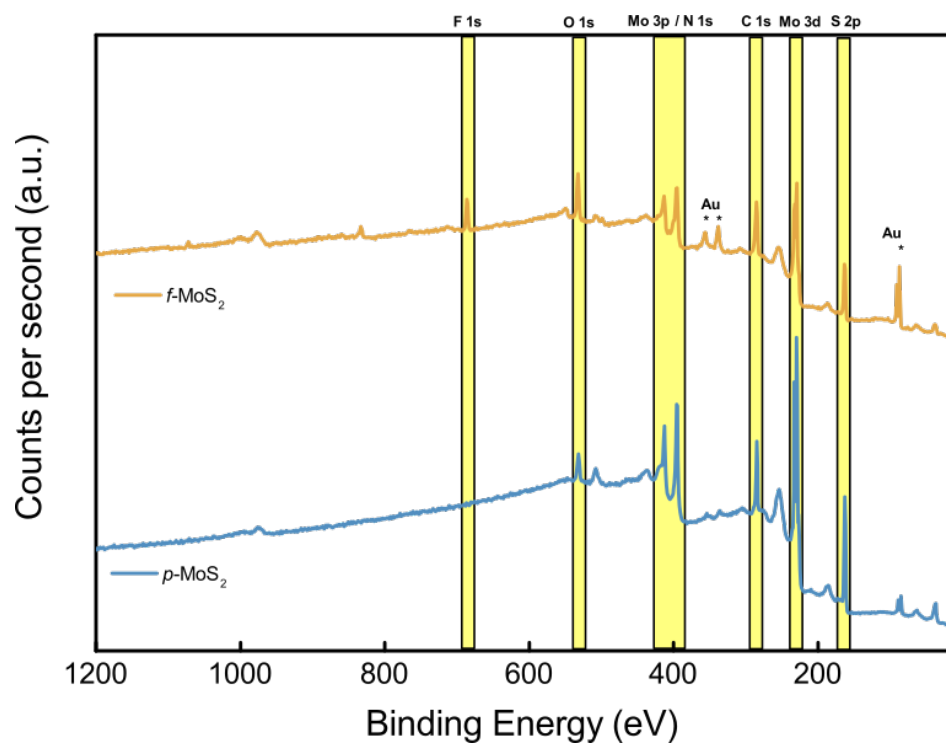
Supplementary Figure 7. ATR-IR of **1** (black trace) and **1** after collection from the reaction with *p*-MoS₂ (yellow trace).



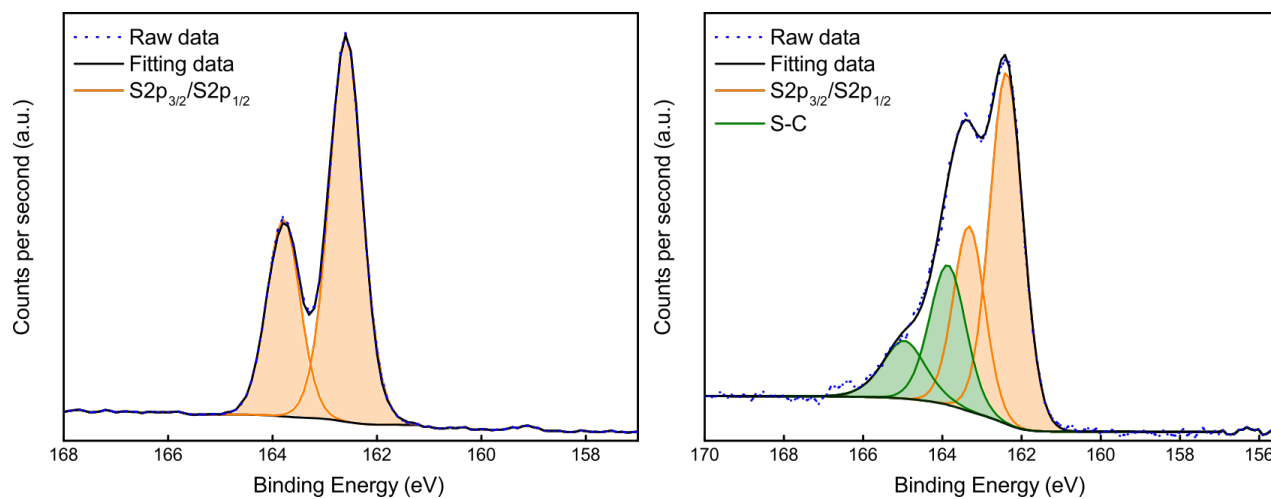
Supplementary Figure 8. TGA profiles and its first derivative (dash line), (air, 10 °C min⁻¹) of pristine MoS₂ and functionalized MoS₂.

Table S1. Atomic percentages of XPS survey of *p*-MoS₂ and *f*-MoS₂.

| Materials | Core level | Binding Energy (eV) | Atomic % |
|----------------------------|------------|---------------------|----------|
| <i>f</i> -MoS ₂ | F 1s | 686.8 | 2.4 |
| | O 1s | 532.5 | 11.2 |
| | N 1s | 400.6 | 1.3 |
| | C 1s | 284.8 | 45.6 |
| | Mo 3d | 229.5 | 12.0 |
| | B 1s | 194.6 | 0.6 |
| | S 2p | 162.3 | 26.9 |
| <i>p</i> -MoS ₂ | O 1s | 531.8 | 5.7 |
| | C 1s | 284.8 | 32.9 |
| | Mo 3d | 229.8 | 19.3 |
| | S 2p | 162.6 | 42.1 |

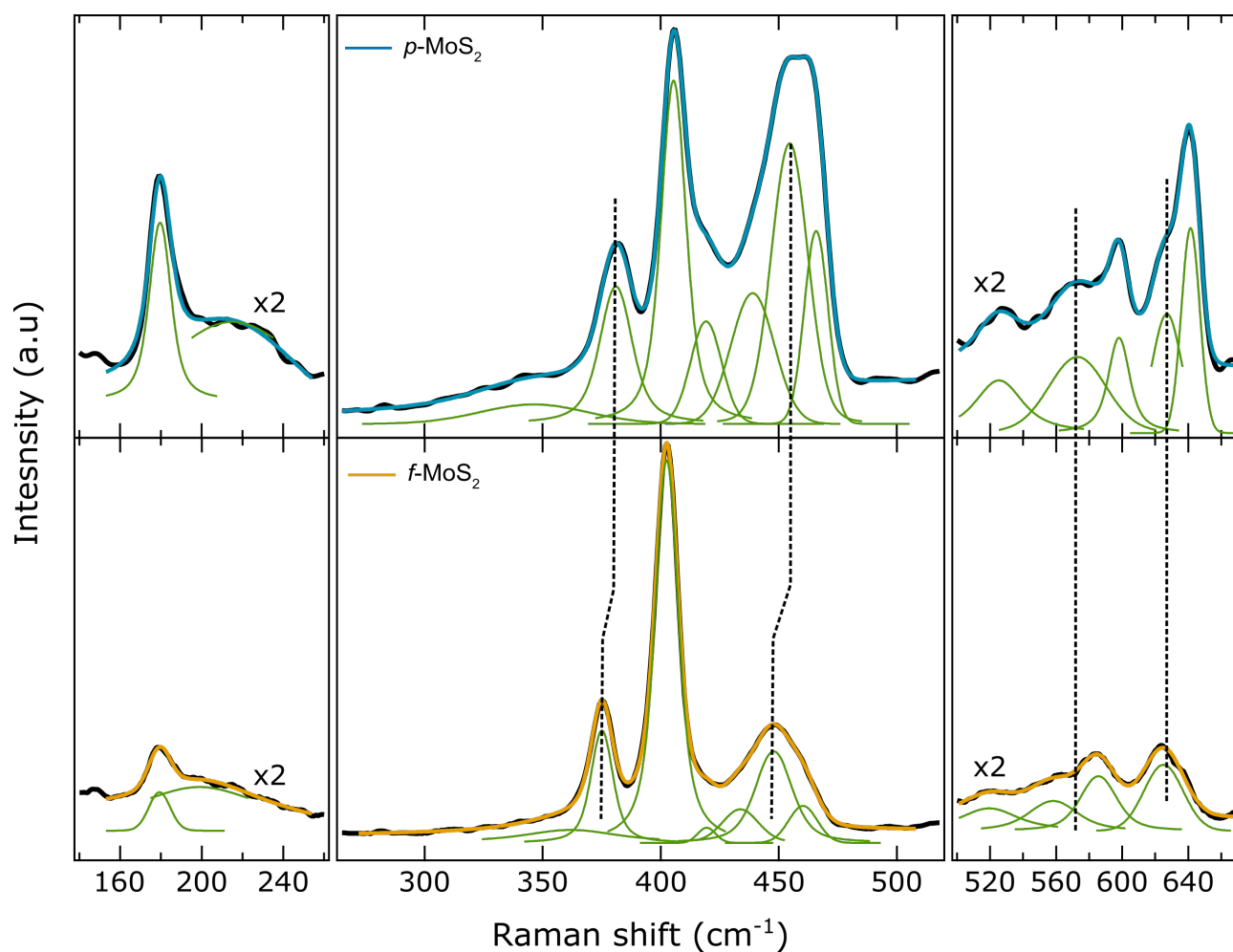


Supplementary Figure 9. XPS survey spectra of *p*-MoS₂ and *f*-MoS₂.

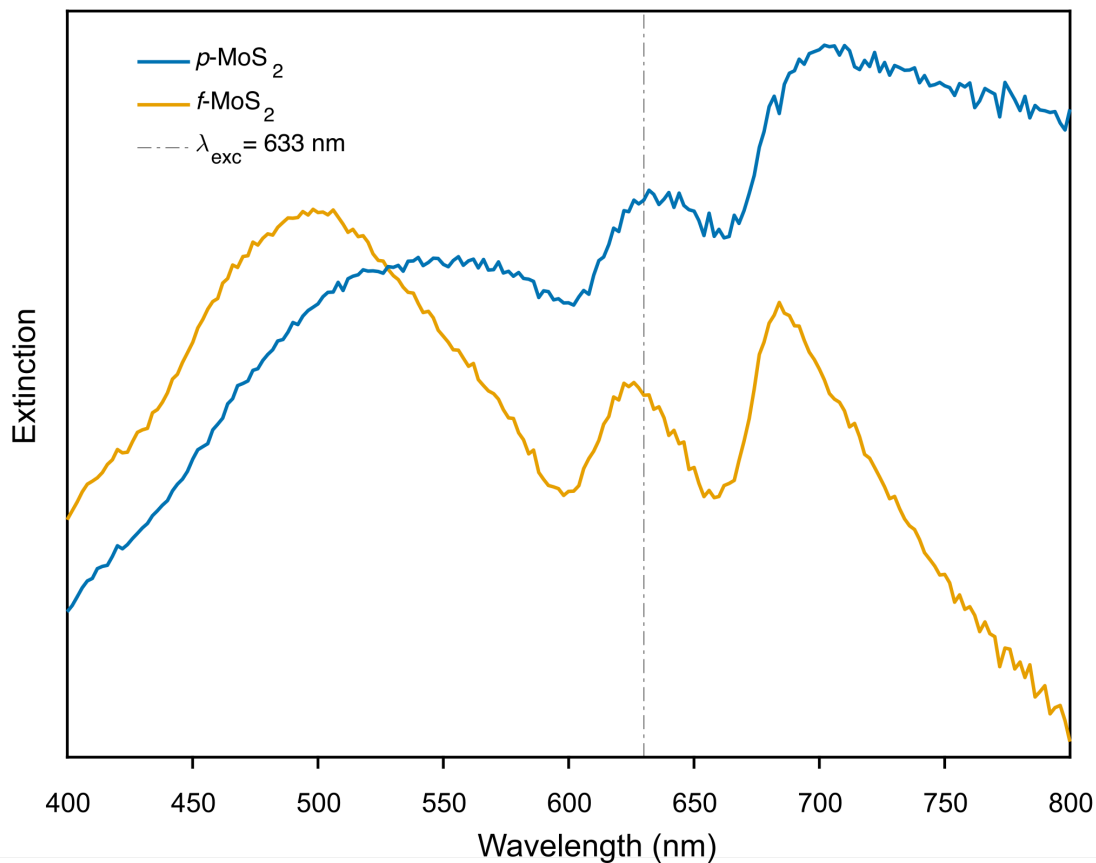


Supplementary Figure 10. XPS core levels of S 2p of *p*-MoS₂ (left), and *f*-MoS₂ (right).

Conventional Raman spectra



Supplementary Figure 11. Fitted curve of conventional Raman spectra from pristine (blue) and functionalized (orange) MoS_2 with **1**. Experimental spectra are shown in black, details of fitted peaks are represented in green. Dotted lines are guides to the eye.



Supplementary Figure 12. UV-Vis absorption spectra of pristine (blue) and functionalized (orange) MoS₂.

Conventional Raman spectra shown in Figure 1c (main text), were acquired at 633 nm. After normalization of the spectra to the A_{1g} mode, free fits were performed with IgorPro in different spectral regions (153-254 cm⁻¹, 272-508 cm⁻¹ and 501-693 cm⁻¹) assuming a linear background and Voigt type peaks. Details of the fittings are shown in Supplementary Figure 11 and fitting results for each peak are presented in Table S2. The intense peaks at ca. 380 and 405 cm⁻¹ are first-order E'_{2g} (in plane) and A_{1g}(out-of-plane) modes, respectively. The rest of the spectral features are related to higher order resonant Raman modes, due to the matching of the excitation laser photon energy with an absorption peak in the UV-Vis spectra attributed to the A exciton in MoS₂ (Supplementary Figure 12).^{2,3,4,5}

The broad spectral feature around 450 cm^{-1} is fitted with 4 individual peaks, following previous detailed analysis of the spectral region.⁶ These peaks are generally assigned to a second-order process involving the longitudinal acoustic phonon at the M point (LA(M)), and the rest of the resonant features to multiphonon bands involving the LA(M) and other phonons at the M point. However, the resonant spectrum of MoS₂ is not fully understood and some controversy on specific peak assignment can be found in literature.^{4,6,7,8,9} A detailed analysis on the origin of each mode is beyond the scope of this work and the assignment presented in Table S2 is based on references the work of Windom,³ Chen¹⁰ and Stacy.¹¹

The main difference between the Raman spectra of pristine and functionalized MoS₂ is an overall reduction of intensity of all resonant modes with respect to the A_{1g} mode. Specifically, the ratio $I(A_{1g})/I(2LA(M))$ is 2.63 for *p*-MoS₂ and 4.18 for *f*-MoS₂, taking the most intense peak in the 450 cm^{-1} region. The ratio $I(A_{1g})/I(A_{1g}(M) - LA(M))$ is 3.71 and 19.22 for *p*- and *f*-MoS₂, respectively. A change in the resonant conditions upon functionalization (confirmed by a shift of the A exciton energy in the UV-Vis spectra of Supplementary Figure 12) could account for such effect, due to a worse coupling of the laser photons to the phonons in the lattice and hence weaker intensity of the resonant modes.^{5,6} The intensity decrease of the 2LA(M) mode at 450 cm^{-1} (increase of the relative intensity $I(A_{1g})/I(2LA(M))$) upon functionalization of MoS₂ by diazonium salts has been measured before and used as an indicator for the functionalization of MoS₂.

In addition to the intensity changes, several red shifts are observed after functionalization. The E'_{2g}, and 2LA(M) modes are showing the largest shifts between 5 and 7 cm^{-1} (table S1). The position of the Raman bands on MoS₂ depends on several factors such as number of layers, density of defects or dopants, temperature, pressure, polytype, excitation wavelength and polarization etc. as a consequence of changes in resonant conditions and electronic structure of the material.^{12,13} It is, therefore, not surprising that frequency shifts are observed upon functionalization. For example, a downshift of the E'_{2g} mode accompanied of an intensity decrease of the 2LA(M) mode at 460 cm^{-1}

has been observed for monolayer MoS₂ upon defect increase and attributed to phonon confinement effects.¹⁴ A detailed analysis of dispersion relations and electronic structure changes upon functionalization would be needed to rationalize the observed frequency shifts.

It is worth to notice that larger shifts are observed on the spectral region around 600 cm⁻¹, however the peak profiles of *p*- and *f*-MoS₂ are rather different and correlation between them cannot be done unambiguously except for the case of the band at 627 cm⁻¹ which does not show a substantial shift upon functionalization (see vertical dotted lines in right panel of Supplementary Figure 11). Interestingly, a sharp and intense peak at 642 cm⁻¹ is detected on the pristine sample and absent on the functionalized one. This mode is assigned to A_{1g}(M)+LA(M) and hence closely related to the peak at 179 cm⁻¹, which is strongly suppressed in the *f*-MoS₂ as well. A large shift is also observed on the shoulder at 215 cm⁻¹, however this shift could be an artifact from the fitting routine due to the weak intensity and broad profile of the peak.

Table S2. Summary of fitting results of conventional Raman spectra in Supplementary Figure 11 and corresponding peak assignment based on the work of Windom,³ Chen¹⁰ and Stacy.¹¹

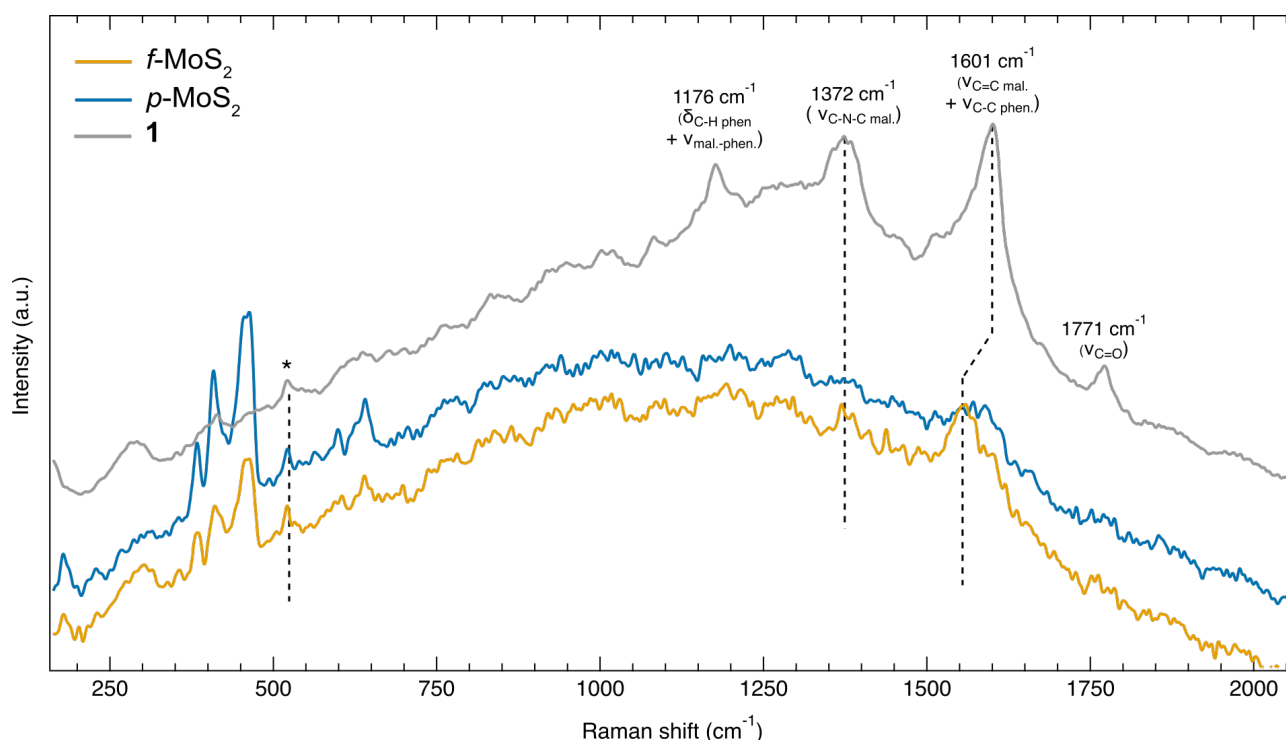
| Mode Assignment | Position | | | Intensity | |
|---------------------------|----------------------------|----------------------------|-------------|----------------------------|----------------------------|
| | <i>p</i> -MoS ₂ | <i>f</i> -MoS ₂ | $\Delta\nu$ | <i>p</i> -MoS ₂ | <i>f</i> -MoS ₂ |
| A _{1g} (M)-LA(M) | 179.6 | 179.3 | 0.3 | 0.234 | 0.050 |
| | 215.0 | 198.8 | 16.2 | 0.104 | 0.056 |
| | 346.2 | 361.9 | -15.7 | 0.049 | 0.033 |
| E' _{2g} | 381.0 | 375.0 | 5.9 | 0.348 | 0.282 |
| A _{1g} | 405.4 | 402.5 | 2.9 | 0.869 | 0.961 |
| | 419.2 | 419.4 | -0.3 | 0.266 | 0.039 |
| 2LA(M) | 438.9 | 433.7 | 5.2 | 0.331 | 0.084 |
| | 454.5 | 447.8 | 6.7 | 0.710 | 0.230 |
| | 465.8 | 460.2 | 5.6 | 0.488 | 0.093 |
| E _{1g} +LA(M) | 525.3 | 519.4 | 5.9 | 0.064 | 0.029 |

| | | | | | |
|-------------------|-------|-------|------|-------|-------|
| $2E_{1g}$ | 572.9 | 558.1 | 14.7 | 0.120 | 0.193 |
| $E_{2g}^1+LA(M)$ | 598.0 | 585.6 | 12.4 | 0.116 | 0.070 |
| | 627.1 | 625.0 | 2.1 | 0.144 | 0.085 |
| $A_{1g}(M)+LA(M)$ | 641.4 | | | 0.249 | |

SERS experiments

Due to the low cross section of Raman scattering, detection of molecule (**1**) linked to the MoS₂ is not feasible with conventional Raman spectroscopy. In order to provide additional indication of functionalization, surface-enhanced Raman spectra (SERS) of pristine and functionalized MoS₂ were measured. SERS is based on the generation of highly enhanced near-fields in the vicinity of metallic nanoparticles via localized surface plasmon excitation. The near-fields around the nanostructures act as hot spots enhancing the detection sensitivity of analytes within those nanometric regions by several orders of magnitude (reaching single molecule detection limit).

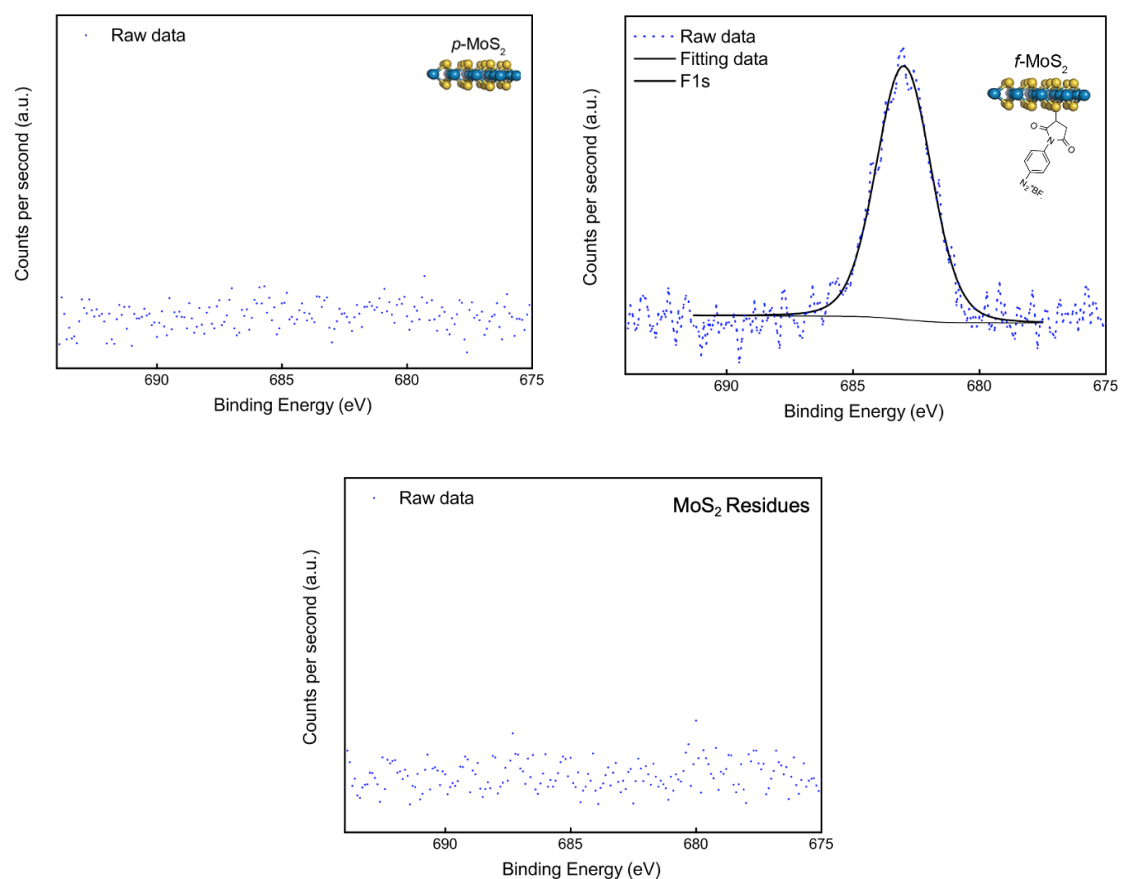
The solid sample/pristine and functionalized flakes were diluted in acetonitrile, sonicated for 10 min and deposited by drop casting on commercial Au SERS substrates (Silmece). The purchased substrates are composed by a nanostructured Si substrate coated with a thin Au film. After deposition of the MoS₂ flakes on the SERS substrates, the microscope of the Raman spectrometer was used to locate thin isolated flakes where Raman mapping was performed (50X objective, 633 nm wavelength, 0.2 mW, 1 sec acquisition). Enhanced Raman signal (characterized by a strong Lorentzian-shaped background increase and a small Raman mode at 520 cm⁻¹ from the silicon in the substrate) was detected only at the boundaries of the analyzed flakes, likely due to reduced thickness at the edges that are better coupled to the nanometric nearfield region. The enhanced spectra from different flakes (3 and 4 different flakes for *f*-MoS₂ and *p*-MoS₂, respectively) were averaged and normalized to the background at 1000 cm⁻¹. A reference SERS experiment of the maleimide molecules alone was also taken. The results are shown in Supplementary Figure 13.



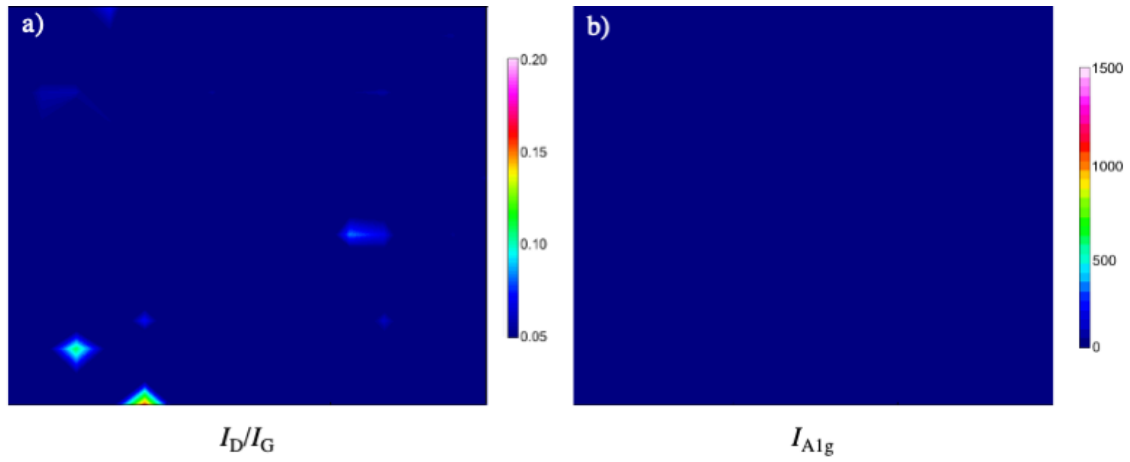
Supplementary Figure 13. Surface enhanced Raman spectra of maleimide (gray), pristine (blue) and functionalized (orange) MoS₂. The asterisk indicates a Raman band from the SERS substrate. Spectra are normalized to the intensity of the background at 1000 cm⁻¹, and offset for clarity. δ : bending, ν : stretch, mal.: maleimide, phen.:phenyl.

A sharp and weak peak at 520 cm⁻¹ belonging to the SERS substrate provides a solid indication that the recorded signal is indeed enhanced in the 3 presented spectra. Three broad and intense peaks dominate the maleimide reference spectrum at 1176 (phenyl C-H in-plane bend or/and maleimide-phenyl stretch), 1372 (maleimide symmetric C-N-C stretch) and 1601 cm⁻¹ (maleimide C=C stretch or/and phenyl symmetric C-C stretch).¹⁵ Additional weaker bands appear at 1083 (maleimide C-H symmetric in-plane bend) and 1771 cm⁻¹ (symmetric C=O stretch). The Raman modes from the MoS₂ are detected in both *p* and *f*-MoS₂ samples. An intense a broad peak at 1557 cm⁻¹ possibly coming from the bonded succinimide molecules at the MoS₂ flakes is detected in the *f*-MoS₂ sample and absent in the pristine case. Note that the broad and weak bump at 1589 cm⁻¹ observed in the pristine

spectrum is assigned to the acetonitrile used as a solvent for deposition on the SERS substrates and is also present as a shoulder in the functionalized case.

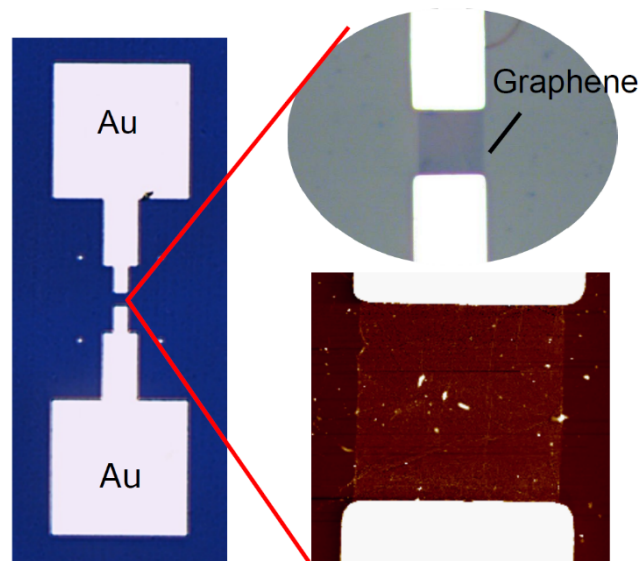


Supplementary Figure 14. XPS core levels of F 1s of *p*-MoS₂, *f*-MoS₂, and the *f*-MoS₂ residues after the reaction with CVDG in presence of water.

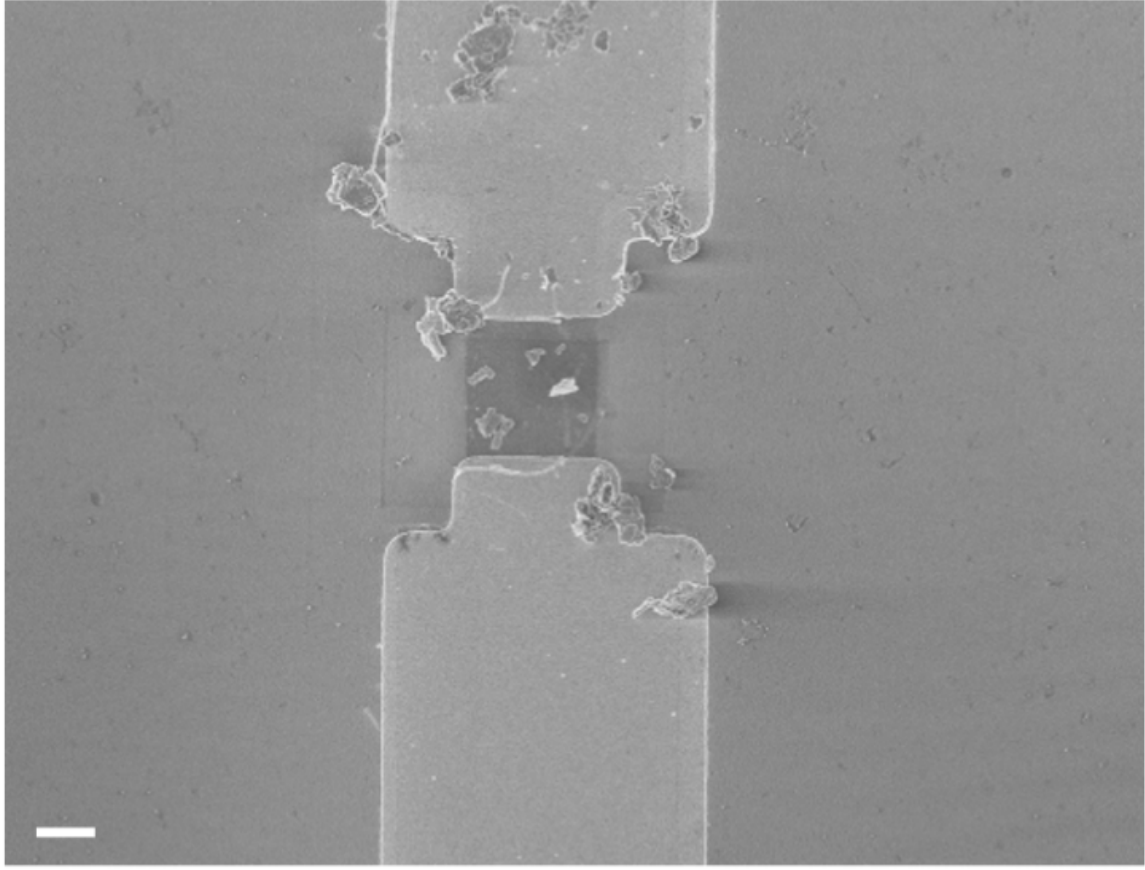


Supplementary Figure 15. a) I_D/I_G (λ_{exc} 532 nm) and c) I_{A1g} (λ_{exc} 532 nm) 2D Raman mapping of a 21 x 24 μm area of CVDG before the functionalization.

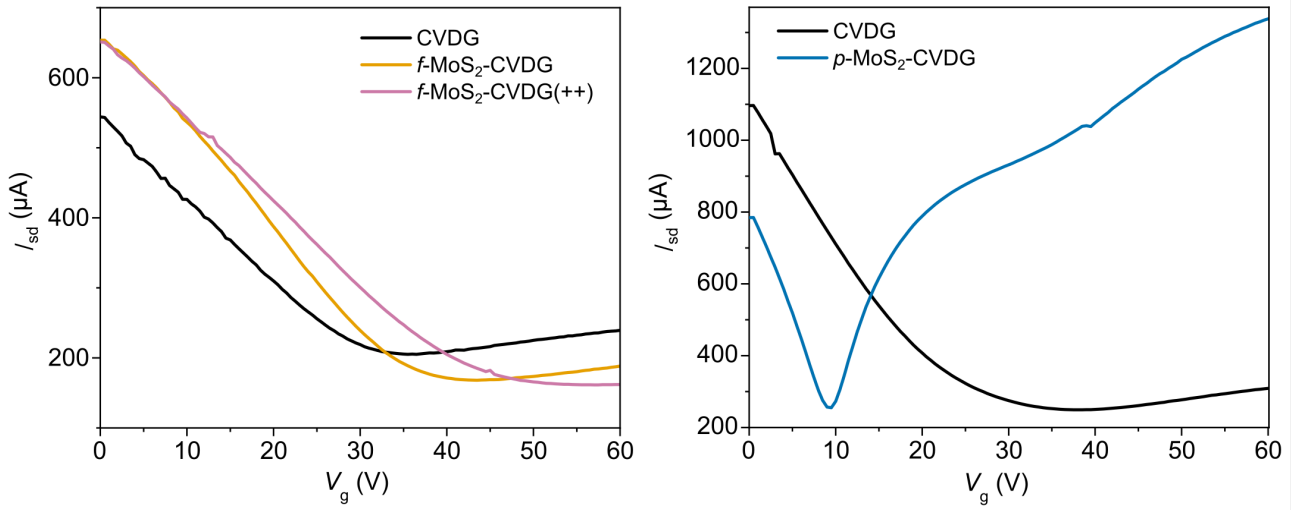
3. Characterization of *f*-MoS₂/CVDG device



Supplementary Figure 16. Optical microscope and AFM image of a graphene 10x10 μm Field-Effect Transistor.



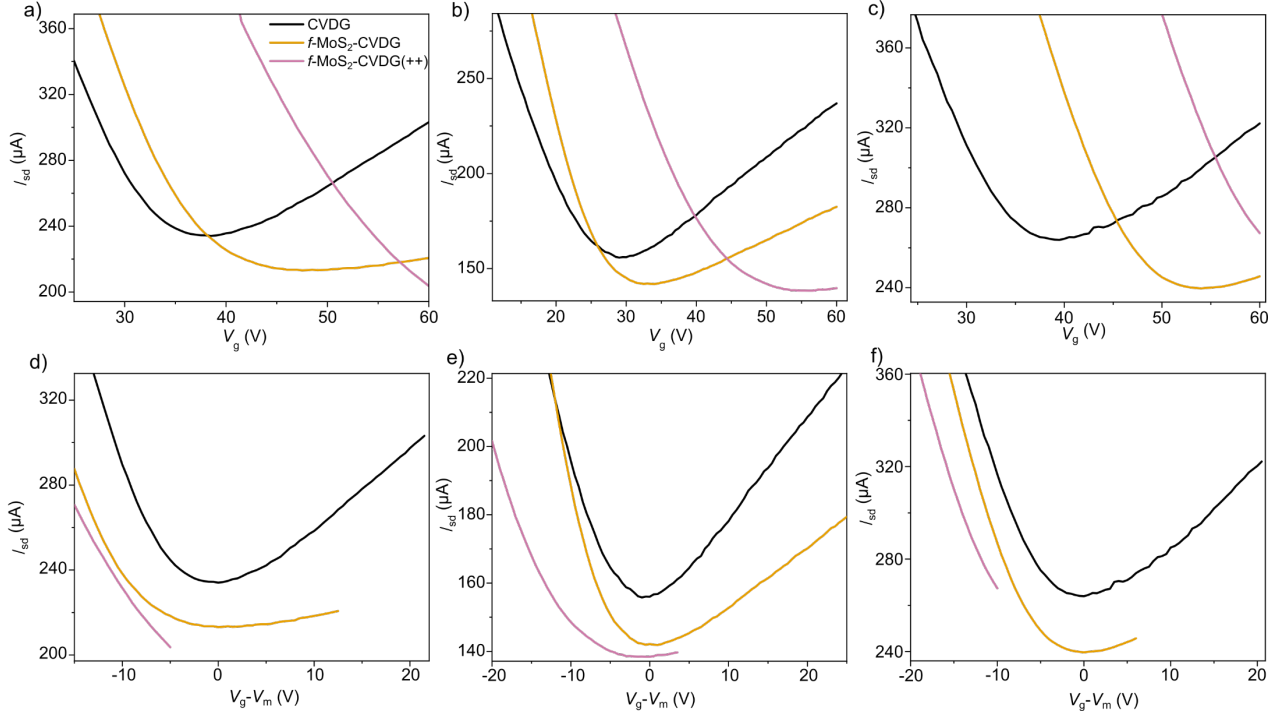
Supplementary Figure 17. SEM of the covalent heterostructure $f\text{-MoS}_2/\text{CVDG}$, $2\mu\text{m}$ scale bar.



Supplementary Figure 18. Full gate voltage characteristics (I_{sd} - V_g) measured on a) the CVDG-FET and $f\text{-MoS}_2\text{-CVDG}$, and b) CVDG-FET and $p\text{-MoS}_2\text{-CVDG}$ shown in Figure 3 of the main text.

Additional electron transport measurements and full-scale gate voltage traces

Supplementary Figure 19 shows the gate voltage characteristic of three additional representative devices. The main electronic characteristics (doping, mobilities, minimum current and shape) after the functionalization with *f*-MoS₂ are qualitatively reproducible from device to device.

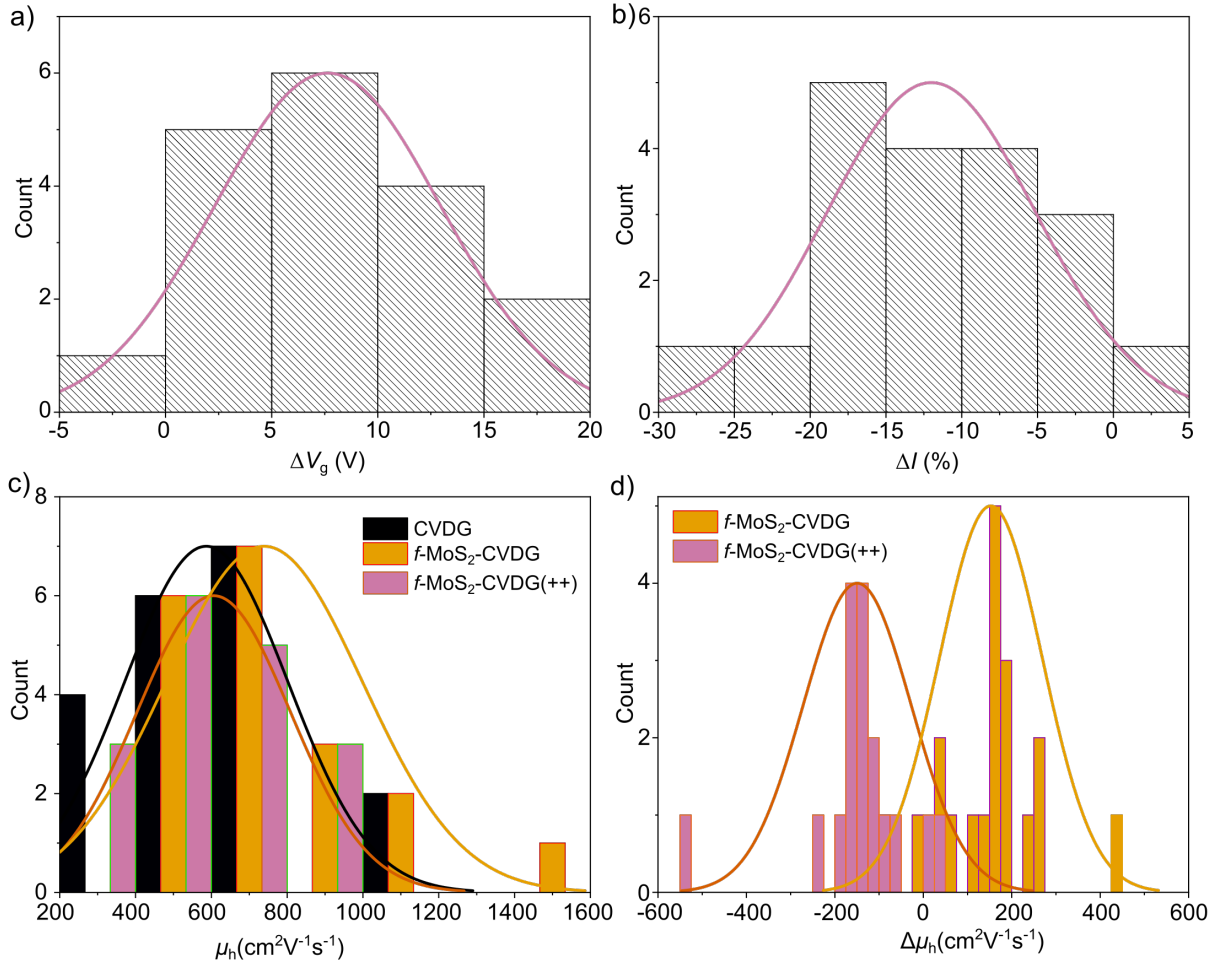


Supplementary Figure 19. a) b) c) Gate voltage characteristics (I - V_g) measured on three different devices on a pristine graphene FET (red), the same device after two hours functionalization with *f*-MoS₂ (pink), and further two hours functionalization (purple). d) e) f) The same gate voltage characteristics renormalized to the V_g potential at the cone minimum V_m .

Statistics on the electron transport measurements

Supplementary Figure 20a and b shows the histograms of the V_g shift and the I shift at the Dirac cone minimum after a first functionalization of 19 graphene FET devices with *f*-MoS₂. The variation shows narrow distributions in V_g shift (doping) and I -shift (covalent bonds) of the cone. The average values and the width of the distribution obtained from the fits to the histograms are: $\Delta V_{g,av} = 7.6 \pm 5.3$ V, ΔI_{av}

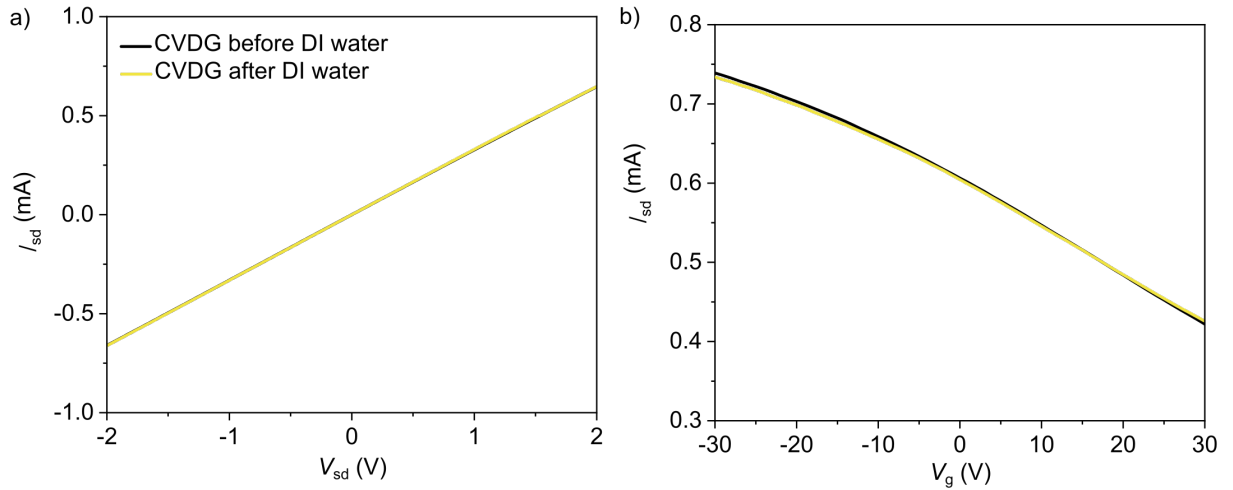
$= -12 \pm 7 \%$. Only one device shows the opposite behaviour with a negative shift of V_g and a positive shift (upshift) of I . The functionalization of the 19 devices on the substrate is therefore rather homogeneous.



Supplementary Figure 20. a), b) Histograms of the a) V_g variation (ΔV_g) and the I variation (ΔI) of the Dirac cone minimum after a first $f\text{-MoS}_2$ functionalization of 19 devices, c) Histogram of hole mobility (μ_h) in 19 pristine graphene FET devices and the same devices after a first and a second functionalization with $f\text{-MoS}_2$ d) Histogram of the hole mobility variation ($\Delta\mu_h$) after a first and a second functionalization obtained from c. The curves are the fits to the distributions.

Supplementary Figure 20c shows the histogram of the hole mobility μ_h of the 19 graphene FET devices and after a first and a second functionalization with the *f*-MoS₂ flakes. Supplementary Figure 20d shows the histogram of the variation in the mobility after the first and second functionalization obtained from Supplementary Figure 20c. The variation after the second functionalization is calculated with respect to the first functionalization. It is interesting to note that the average mobility increases after the first functionalization $\Delta\mu_{h,av} = 152 \pm 116 \text{ cm}^2\text{V}^{-1}\text{s}^{-1}$ whereas decreases after the second functionalization $\Delta\mu_{h,av} = -149 \pm 121 \text{ cm}^2\text{V}^{-1}\text{s}^{-1}$, still remaining above the initial μ_h in pristine graphene FETs.

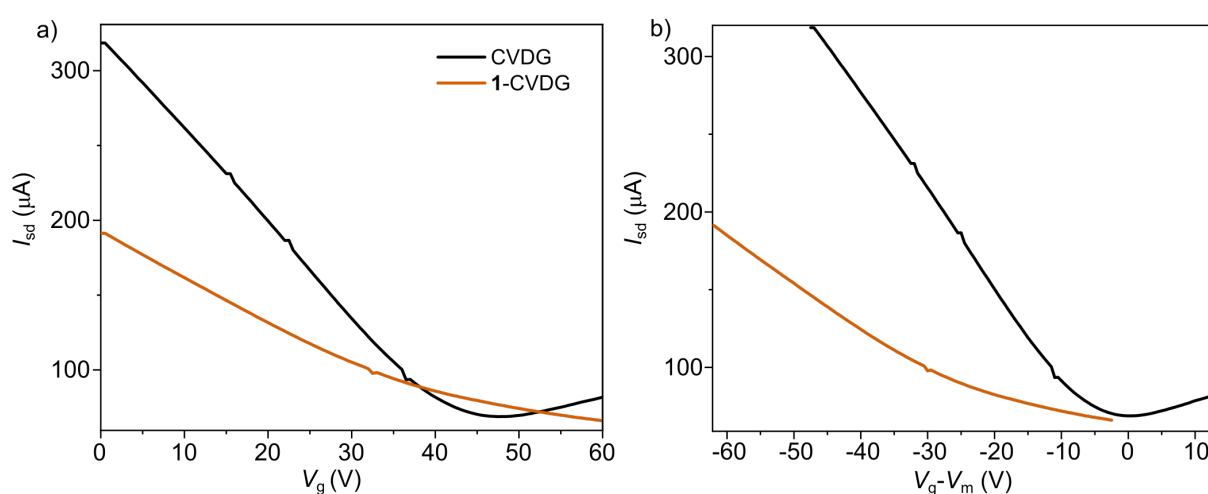
Control experiment with DI water



Supplementary Figure 21. a) Current-voltage characteristic (I_{sd} - V_{sd}) and b) gate voltage characteristic measured on a pristine CVDG-FET device and the same device after dropcasting DI water followed by a thermal annealing. No significant change in the current is observed.

Electron transport measurements on graphene functionalized with diazonium salts.

Supplementary Figure 22 shows the gate characteristic of a representative pristine graphene FET device and the same device after functionalization with **1**. The characteristics after functionalization follow an opposite trend when compared with the MoS₂-graphene van der Waals heterostructure. First, a clear p-doping effect is observed after functionalization. Second, the hole mobility on graphene drastically decreases. Third, the current at the cone minimum decreases and, finally, the Dirac cone widens significantly. These characteristics are observed in 15 out of 17 (88%) measured devices.

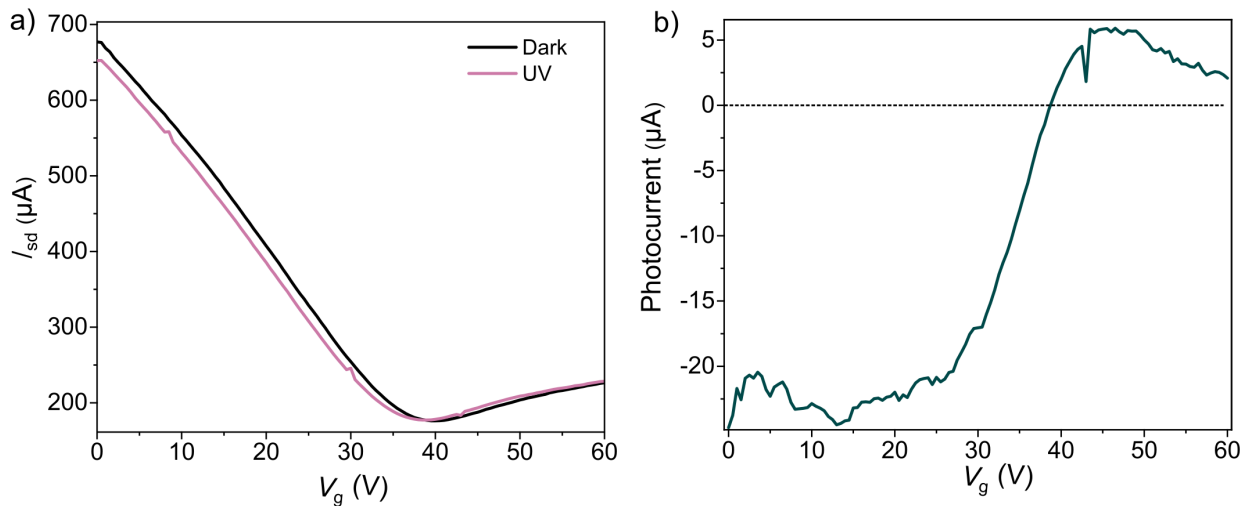


Supplementary Figure 22. a) Gate voltage characteristics (I - V_g) measured on a pristine graphene FET (black), the same device after two hours functionalization with bare diazonium molecules (red). b) The same gate voltage characteristics renormalized to the V_g potential at the cone minimum V_m .

Photoresponsivity of the *f*-MoS₂/CVDG heterostructure

Supplementary Figure 23a shows the gate voltage characteristic measured on a graphene-*f*-MoS₂ FET under dark conditions and when shined with a green (365 nm) laser source. The measurement is performed in vacuum. A clear shift to lower gate voltage is observed when shining with light. The negative shift of the cone seems to indicate that the photoexcited holes generated in the MoS₂ are trapped in the MoS₂ whereas the photoexcited electrons are transferred into graphene.¹⁶ The

photocurrent dependence with the gate voltage is shown in Supplementary Figure 23b. A further analysis should be performed to understand the role of the light power and frequency as well as to discard potential doping effect of adsorbants.



Supplementary Figure 23. a) Gate voltage characteristic measured on a f -MoS₂/CVDG FET heterostructure under dark conditions and illuminated with a green (365 nm) laser. b) Photocurrent as a function of the gate voltage.

4. References

- 1 Lin, Y. C. et al. Clean transfer of graphene for isolation and suspension. *ACS Nano* **5**, 2362-2368, (2011).
- 2 Livneh, T. & Sterer, E. Resonant Raman scattering at exciton states tuned by pressure and temperature in 2H-MoS₂. *Phys. Rev. B: Condens. Matter Mater. Phys.* **81**, 195209/195201-195209/195209, (2010).
- 3 Windom, B. C., Sawyer, W. & Hahn, D. W. A Raman spectroscopic study of MoS₂ and MoO₃: applications to tribological systems. *Tribology Letters* **42**, 301-310, (2011).
- 4 Livneh, T. & Spanier, J. E. A comprehensive multiphonon spectral analysis in MoS₂. *2D Materials* **2**, 035003, (2015).
- 5 Fan, J.-H. et al. Resonance Raman scattering in bulk 2H-MX₂ (M= Mo, W; X= S, Se) and monolayer MoS₂. *Journal of Applied Physics* **115**, 053527, (2014).
- 6 Carvalho, B. R. et al. Intervalley scattering by acoustic phonons in two-dimensional MoS₂ revealed by double-resonance Raman spectroscopy. *Nature communications* **8**, 1-8, (2017).

- 7 Placidi, M. et al. Multiwavelength excitation Raman scattering analysis of bulk and two-dimensional MoS₂: vibrational properties of atomically thin MoS₂ layers. *2D Materials* **2**, 035006, (2015).
- 8 Li, H. et al. From Bulk to Monolayer MoS₂: Evolution of Raman Scattering. *Advanced Functional Materials* **22**, 1385-1390, (2012).
- 9 Knirsch, K. C. et al. Basal-Plane Functionalization of Chemically Exfoliated Molybdenum Disulfide by Diazonium Salts. *ACS Nano* **9**, 6018-6030, (2015).
- 10 Chen, J. & Wang, C. Second order Raman spectrum of MoS₂. *Solid State Communications* **14**, 857-860, (1974).
- 11 Stacy, A. & Hodul, D. Raman spectra of IVB and VIB transition metal disulfides using laser energies near the absorption edges. *Journal of Physics and Chemistry of Solids* **46**, 405-409, (1985).
- 12 Zhang, S. et al. Spotting the differences in two-dimensional materials—the Raman scattering perspective. *Chemical Society Reviews* **47**, 3217-3240, (2018).
- 13 Saito, R. et al. Raman spectroscopy of transition metal dichalcogenides. *J Phys Condens Matter* **28**, 353002, (2016).
- 14 Mignuzzi, S. et al. Effect of disorder on Raman scattering of single-layer Mo S₂. *Physical Review B* **91**, 195411, (2015).
- 15 Parker, S. F. Vibrational spectroscopy of N-phenylmaleimide. *Spectrochimica Acta Part A: Molecular and Biomolecular Spectroscopy* **63**, 544-549, (2006).
- 16 Zhang, W. et al. Ultrahigh-gain photodetectors based on atomically thin graphene-MoS₂ heterostructures. *Scientific reports* **4**, 3826, (2014).